ABSTRACT

SPARSITY BASED METHODS FOR TARGET LOCALIZATION IN MULTI-SENSOR RADAR

by
Haley H. Kim

In this dissertation, several sparsity-based methods for ground moving target indicator (GMTI) radar with multiple-input multiple-output (MIMO) random arrays are proposed. MIMO random arrays are large arrays that employ multiple transmitters and receivers, the positions of the transmitters and the receivers are randomly chosen. Since the resolution of the array depends on the size of the array, MIMO random arrays obtain a high resolution. However, since the positions of the sensors are randomly chosen, the array suffers from large sidelobes which may lead to an increased false alarm probability. The number of sensors of a MIMO random array required to maintain a certain level of peak sidelobes is studied. It is shown that the number of sensors scales with the logarithm of the array aperture, in contrast with a ULA where the number of elements scales linearly with the array aperture. The problem of sparse target detection given space-time observations from MIMO random arrays is presented. The observations are obtained in the presence of Gaussian colored noise of unknown covariance matrix, but for which secondary data is available for its estimation. To solve the detection problem two sparsity-based algorithms, the MP-STAP and the MBMP-STAP algorithms are proposed that utilizes knowledge of the upper bound on the number of targets. A constant false alarm rate (CFAR) sparsity based detector that does not utilize any information on the number of targets referred to as MP-CFAR and MBMP-CFAR are also developed. A performance analysis for the new CFAR detector is also derived, the metrics used to describe the performance of the detector are the probability of false alarm and the probability of detection. A grid refinement procedure is also proposed to eliminate the need

for a dense grid which would increase the computational complexity significantly. Expressions for the computational complexity of the proposed CFAR detectors are derived. It is shown that the proposed CFAR detectors outperforms the popular adaptive beamformer at a modest increase in computational complexity.

SPARSITY BASED METHODS FOR TARGET LOCALIZATION IN MULTI-SENSOR RADAR

by
Haley H. Kim

A Dissertation
Submitted to the Faculty of
New Jersey Institute of Technology
in Partial Fulfillment of the Requirements for the Degree of
Doctor of Philosophy in Electrical Engineering

Helen and John C. Hartmann
Department of Electrical and Computer Engineering

January 2017

APPROVAL PAGE

SPARSITY BASED METHODS FOR TARGET LOCALIZATION IN MULTI-SENSOR RADAR

Haley H. Kim

Dr. Alexander M. Haimovich, Dissertation Advisor — Date
Distinguished Professor of Electrical and Computer Engineering, NJIT

Dr. Osvaldo Simeone, Committee Member — Date
Professor of Electrical and Computer Engineering, NJIT

Dr. Joerg Kliewer, Committee Member — Date
Associate Professor of Electrical and Computer Engineering, NJIT

Dr. Ali Abdi, Committee Member — Date
Professor of Electrical and Computer Engineering, NJIT

Dr. Mark A. Govoni, Committee Member — Date
Chief Scientist, US Army CERDEC I2WD

BIOGRAPHICAL SKETCH

Author: Haley H. Kim

Degree: Doctor of Philosophy

Date: January 2017

Undergraduate and Graduate Education:

- Doctor of Philosophy in Electrical Engineering,
  New Jersey Institute of Technology, Newark, NJ, 2017
- Master of Science in Electrical Engineering,
  New Jersey Institute of Technology, Newark, NJ, 2012
- Bachelor of Science in Electrical Engineering,
  New Jersey Institute of Technology, Newark, NJ, 2011

Major: Electrical Engineering

Presentations and Publications:

Haley H. Kim and Alexander M. Haimovich, "CFAR Compressive Sensing for STAP Random Arrays," Submitted to *IEEE Trans. on Aerospace and Electron. Syst.*

Haley H. Kim and Alexander M. Haimovich, "Design of CFAR Radars using Compressive Sensing," in *Proc. IEEE Radar Conf.*, pp. 1-6, May, 2016.

Haley H. Kim, Mark A. Govoni, and Alexander M. Haimovich, "Cost Analysis of Compressive Sensing for MIMO STAP Random Arrays," in *Proc IEEE Radar Conf.*, pp. 980-985, May 2015

Haley H. Kim, Alexander M. Haimovich, and Mark A. Govoni, "Sparse Arrays, MIMO, and Compressive Sensing for GMTI Radar," in *Proc IEEE Radar Conf.*, pp. 849-853, May 2015

Haley H. Kim, Alexander M. Haimovich, and Yonina C. Eldar, "Non-Coherent Direction of Arrival Estimation from Magnitude-Only Measurements," *IEEE Signal Process. Letters*, vol. 22, no. 7, pp. 925-929, 2015

Dedicated to the Educational Opportunity Program (EOP). The group of people who made it their goal to help underrepresented people realize that they have the ability to succeed. Without EOP, I could never have succeeded in this academic journey. I want to thank EOP for allowing me to be a part of their family, and hope that I can become an example of what an EOP student can become.

ACKNOWLEDGMENT

I would like to first express my gratitude to Professor Alexander M. Haimovich for the opportunity to pursue my PhD degree, funding my research, and his valuable guidance. The advice I have received from Alex was invaluable and critical to my growth as a scientist.

I would also like to express my gratitude to Professors Osvaldo Simeone, Ali Abdi, and Joerg Kliewer as well as Dr. Mark Govoni for serving as my committee members. I personally would like to thank Professor Simeone for sharing his deep technical mathematical knowledge through his advanced level courses at NJIT.

I also want to thank all my colleagues at NJIT, who went on this academic journey with me. In particular I'd like to thank Nil, Marco, Wei, Annan, Phouc, Eric, Liu, and Pelin. I'd also like to thank Angela Retino and Kathy Bosco for their friendship over the years and their help with all the administrative matters during my PhD studies.

I'd like to thank my friends, Travis Talboys, Danny Hy, Daniel Casey, John McGimpsey, Cristin DeSaro, Jose Guerrero, and Miranda Garza for their incredible support and friendship over the years. Lastly, I want to thank my mother Irene Yoon, my father, Chris Kim, my brother Chris Kim and my girlfriend Yingyu Mao for their constant support and understanding.

TABLE OF CONTENTS

TABLE OF CONTENTS
(Continued)

Chapter **Page**

LIST OF FIGURES

LIST OF FIGURES
(Continued)

Figure **Page**

LIST OF FIGURES
(Continued)

Figure **Page**

CHAPTER 1

INTRODUCTION

Ground moving target indication (GMTI) radar [1]–[5] is an airborne radar tasked with detecting the presence of moving targets in an environment where the interference due to ground clutter can be severe. GMTI radars therefore is expected to be able to perform target detection while suppressing the interference due to ground clutter. The ground clutter as seen by the airborne radar, exists at every angle, in addition, due to the platform velocity of the aircraft, the ground clutter also exists for all Dopplers. Adaptive array processing techniques that perform only spatial or Doppler filtering is therefore unsuited for GMTI radar. Viewed in the two dimensional angle-Doppler map, the clutter response exhibits a response in what is known as the clutter ridge [6], [7] illustrated in Figure 1.1.

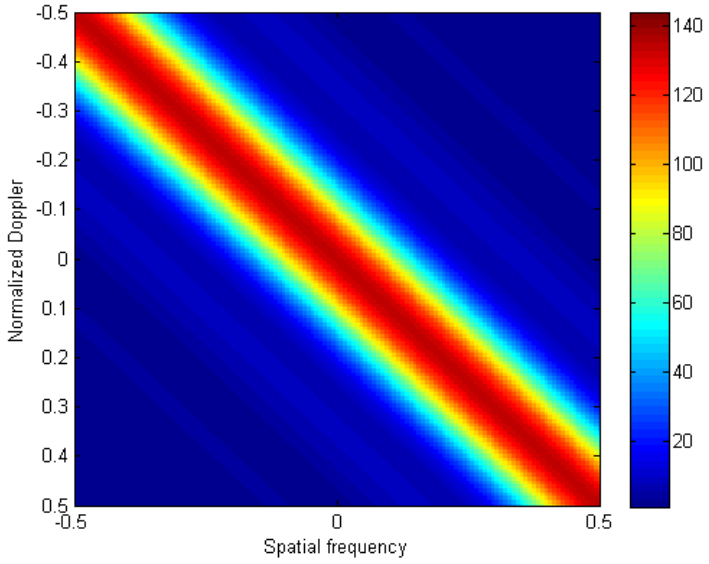

Figure 1.1 Illustration of the clutter ridge in the angle-Doppler map.

To take advantage of the structure of the clutter ridge, researchers have considered space-time adaptive processing (STAP) [8]–[10], which performs joint

processing in both spatial and temporal domains simultaneously. Since the clutter does not occupy the entire angle-Doppler map, separating the target from the clutter is possible with STAP, assuming that the target is sufficiently far from the clutter ridge on the angle-Doppler map. However, slow moving targets that lie in regions close to the clutter ridge may be masked by the ground clutter. Hence, GMTI radars may experience difficulties discriminating a slow moving target from the clutter.

One approach to improving the detection of slow moving targets is to employ an array with a large aperture length [11]. This can be achieved by the use of a large uniform linear array (ULA) where the inter-element spacing of the array is $\lambda/2$ where λ is the radar operating carrier wavelength. The large ULA offers improved angle-Doppler resolution, this improved resolution causes the clutter ridge to become narrower therefore improving the ability to discriminate between the clutter and slow moving targets. In addition, large ULAs offers the radar low sidelobes levels [12]–[14] which allows the radar to maintain a constant false alarm rate (CFAR). Unfortunately, since the inter-element spacing of the array is fixed to $\lambda/2$, the number of elements required to fill a ULA scales linearly with the aperture of the array. This means that large ULAs require a large number of elements and are expensive and often infeasible to employ for GMTI radars due to constraints on the equipment size, weight, and power.

Instead of using a large ULA and localizing targets by beamforming [15], one may consider a smaller ULA, but use more sophisticated localization algorithms, such as Capon's method [16], MUSIC [17]–[19], or ESPRIT [20]–[22]. All three methods are capable of resolving targets within the Rayleigh resolution limit, whereas conventional beamformering cannot. MUSIC and ESPRIT however, require knowledge of the number of targets. This information is rarely known to a radar and must be obtained by other means, such as using the Akaike information criteria (AIC) or the minimum description length (MDL) [23]–[25]. Unfortunately, such methods do not allow one

to control the false alarm rate, a basic requirement in radar. In addition, all three methods require multiple observations of each resolution cells which is typically not available in STAP applications.

To reduce the number of elements needed for a high resolution radar one may use a multiple-input multiple-output (MIMO) radar [26]–[31]. In MIMO radar, one uses M transmitters to transmit M orthogonal waveforms, the returns from the M waveforms are collected by N receive elements generating MN measurements. It is known that if the N receive elements are spaced by $\lambda/2$ and the M transmitters are space by $N\lambda/2$ the radar behaves as if it was a ULA with MN elements. Since the MIMO radar behaves like a ULA, the sidelobes of the array beampattern are small, in addition, the MIMO radar depends on the product MN instead of just N. Unfortunately, the MIMO radar suffers from the same drawbacks of a large ULA, the number of elements MN scales linearly with the aperture of the array.

An alternative approach to increasing the resolution of a radar without using a large number of sensors is to use a large random array. In random arrays [32]–[35], one randomly position sensors across a large array aperture. Since the resolution of the radar depends mostly on the size of the aperture [32] this allows the radar to achieve high angular resolution while employing a small number of sensors. Unfortunately, the random array does not come without drawbacks. Due to the spatial undersampling, the array beampattern suffers from high sidelobes. In particular, in [32], it was shown that the sidelobe that the average sidelobe level of the array is inversely proportional to the number of elements. Since the goal of a random array is to utilize a small number of elements, for most cases of interest, the average sidelobe level is typically quite large.

In this dissertation, a radar architecture is formed by combining the MIMO array with the random array, this radar architecture is referred to as a MIMO random array [36], [37]. In MIMO random arrays, one randomly positions both transmit and

receive sensors across a large array aperture. By employing multiple transmit elements along with the receive elements of a random array, one may increase the number of measurements available to the radar from N to MN. The increase in the number of measurements may potentially decrease the sidelobe level. Unfortunately, even with the increased number of measurements from a MIMO random array, high sidelobes are an unavoidable characteristic. During the beamforming stages of STAP, these higher sidelobes may cause a significant increase in false alarms [38].

Interestingly however, in [36], [37] the authors show that compressive sensing (CS) techniques [39], [40] tailored for sparse localization can cope with the spatial undersampling of a MIMO random array. This allows the user to reap the full benefits of a large MIMO random array without worrying that the high sidelobes will unnecessarily increase the false alarm rate. In addition, CS techniques applied to localization was shown to be capable of resolving targets within the Rayleigh resolution limit [41]–[43]. The goal of all CS techniques is to recover the signal of interest $\mathbf{x}$ given the received data vector $\mathbf{y}$ which is expressed as $\mathbf{y} = \mathbf{A}\mathbf{x} + \mathbf{e}$, where $\mathbf{A}$ is the measurement matrix and $\mathbf{e}$ is an interference vector. If the signal $\mathbf{x}$ is known to be sparse (i.e. contains few nonzero elements), CS states that to find the *sparsest* solution one needs to solve the nonconvex optimization problem

$$\min_{\mathbf{x}} \|\mathbf{y} - \mathbf{A}\mathbf{x}\|_2^2 + \lambda \|\mathbf{x}\|_0$$

where $\|\mathbf{x}\|_0$ counts the numbers of nonzeros in $\mathbf{x}$. The term λ governs the trade-off between minimizing the term ($\|\mathbf{y} - \mathbf{A}\mathbf{x}\|_2^2$) and the term that reduces the sparsity of the solution ($\|\mathbf{x}\|_0$).

Unfortunately, since the above optimization problem is nonconvex, only approximate solutions can be obtained. One approach to obtaining an approximate solution is to apply a convex relaxation, this approach is referred to as basis pursuit

(BP). Algorithms such as those in [39], [44]–[48] approximate the nonconvex penalty term $\|\mathbf{x}\|_0$ with the convex penalty term $\|\mathbf{x}\|_1$. The result is a convex optimization problem which can be solved by using various solvers in polynomial time. In [41], [49] the authors use this approach to solve the sparse localization problem. In doing so, the authors were able to show that BP is able resolve targets within the Rayleigh resolution limit like MUSIC and ESPRIT, but doesn't require multiple snapshots. Unfortunately, the authors were unable to explain how to design a constant false alarm rate (CFAR) radar using BP. The authors in [50] argued that a CFAR radar can be obtained by properly designing the parameter λ. However, in [51] the authors point out that the output noise distribution is unknown and unpredictable which makes BP unsuitable for CFAR radars.

On the other hand algorithms such as those in [52]–[56] are greedy algorithms that iteratively search for targets one by one. These greedy algorithms are often referred to as matching pursuit (MP) algorithms. Although MP generally has weaker guarantees than BP, it has been shown empirically that it often performs similarly to that of BP and in some cases even outperforms BP [57]. The most substantial advantage in using MP algorithms as opposed to BP algorithms is their computational complexity [**?**] which is comparable to that of the beamformer [58]. Although an enormous amount of papers have considered the use of MP algorithms for radar, only the authors in [55] have considered a detection algorithm using MP to design a CFAR radar. However, the detection algorithm in [55] only considers the case where measurements are corrupted by white Gaussian noise and requires knowledge on the number of targets. In particular, although the number of targets is not available, the authors in [55] assumes that an upper bound on the number of targets $\overline{K}$ is available. The authors then use MP to find $\overline{K}$ angle-Doppler cells to test for the presence of a target and uses a CFAR detector to perform the test for the $\overline{K}$ cells. However, the computational complexity of MP increases as $\overline{K}$ increases [52, 36]. This increase in

computational complexity may be unsuitable for STAP where the dimensions of the data can range from several hundred to several thousands depending on radar system being used [6].

In addition to these short comings, the authors in [55] assumed that the targets comply with a grid of discretized points. However, in STAP, target parameters are specified in a two-dimensional continuous domain, not a discretized one. In reality, targets almost never comply with a grid of discretized points and targets often lie off the grid regardless how fine the granularity of the grid becomes. When targets do not comply with the discrete grid of angle-Doppler points it was shown that the performance of both BP and MP based algorithms may degrade significantly [59]–[61]. Numerous techniques have been proposed in literature [62]–[68] to mitigate the effects of off-grid targets. The most straightforward method to handle off-grid targets is to simply increase the number of grid points sampled on the angle-Doppler map. This method, although simple, increases the computational complexity of MP algorithms since the computational complexity increases linearly with the number of grid points. Additionally, the use of very fine grids may lead to numerical instability issues. In [62, 65, 66] the authors propose approximate the nonconvex penalty term $\|\mathbf{x}\|_0$ with the convex penalty term $\|\mathbf{x}\|_{\mathcal{A}}$ where $\|\mathbf{x}\|_{\mathcal{A}}$ refers to the *atomic norm* (more details on the atomic norm can be found in [69]). The resulting optimization problem is convex and can be solved by a convex solver in polynomial time. Similar to BP, the computation time required to solve the optimization problem proposed in [62] is too large for radar applications. The authors in [63] proposed a matrix completion algorithm to mitigate the effects of off-grid targets. However, the authors noted that the matrix completion algorithm requires the same computation time as the optimization problem in [62] and therefore impractical for radar applications.

This dissertation focuses on the detection of targets for GMTI radar using a large MIMO random array. The large MIMO random array allows one to obtain

a high resolution radar with a low number of transmitters and receivers. The high resolution of the array allows one to detect slow moving targets but comes at the cost of high sidelobes. CS techniques are utilized to cope with the high sidelobes of the MIMO random array. In particular, a sparsity based CFAR detector is developed that iteratively finds targets one by one and removes detected targets from the observations for the detection subsequent targets to reduce the interference between targets. The CFAR detector is then modified with a grid refinement procedure so that it may handle targets that lie off the grid. An analysis of the computational complexity of the proposed CFAR detector is also presented.

The contributions of this dissertation are the following:

1. Show that the number of elements of a MIMO random array required to maintain a certain level of peak sidelobes scales with the logarithm of the array aperture, in contrast with a ULA where the number of elements scales linearly with the array aperture.

2. Formulate the problem of sparse target detection given space-time observations from random arrays. The observations are obtained in the presence of Gaussian colored noise of unknown covariance matrix, but for which secondary data is available for its estimation.

3. Extend the detector in [55] for GMTI radar. The detector removes contributions from previously detected targets from the observations to reduce interference between targets. The detector is given knowledge of the upper bound on the number of targets.

4. Develop a new CFAR detector such that previously detected targets are removed from the observations to reduce interference between targets. The developed CFAR detector does not require *any* information about the number of targets.

5. Develop the performance analysis for the new sparsity-based radar detector including expressions for the probability of false alarm and the probability of detection.

6. Propose a grid refinement procedure to handle off-grid targets. The grid refinement procedure also prevents the need to the generate a dense grid which would increase the computational complexity significantly.

7. Develop expressions for the computational complexity of the proposed CFAR detectors.

This dissertation is organized as follows: Chapter 2 presents the signal model, the properties of the clutter is reviewed, and properties of the MIMO random array is presented. In Chapter 3, a sparsity-based radar that utilizes an upper bound on the number of targets is presented. In Chapter 4, a new sparsity-based CFAR detector is presented, the expressions for the probability of false alarm and the probability of detection for the proposed CFAR detector is derived. In Chapter 5, a grid refinement procedure for the proposed detector is presented to handle targets that lie off the grid. The computational complexity of the proposed sparsity-based CFAR detectors are analyzed. In Chapter 6 conclusions are made.

The following notation will be used: boldface is used for matrices (uppercase) and vectors (lowercase); $\|\mathbf{y}\|_p$ denotes p-norm; $(\cdot)^T$ is the transpose operator, $(\cdot)^*$ is complex conjugate and $(\cdot)^H$ is the complex conjugate transpose operator; given a set S, and a matrix $\mathbf{A}$, $|S|$ denotes the cardinality of the set, $\mathbf{A}_S$ is the sub-matrix obtained by the columns of $\mathbf{A}$ indexed in S; similarly, if $\mathbf{x}$ is a vector, the vector $\mathbf{x}_S$ consists of the components of $\mathbf{x}$ indexed by S; $\otimes$ marks the Kronecker product ; $\mathbb{E}[\cdot]$ denotes the expectation operator; $\sim CN(\mathbf{m}, \mathbf{R})$ indicates the complex-valued multivariate Gaussian distribution with mean $\mathbf{m}$ and covariance matrix $\mathbf{R}$.

CHAPTER 2

MIMO RANDOM ARRAYS IN STAP

In this chapter, the signal model that will be used throughout this dissertation is introduced. In addition, some properties of the MIMO random array will be presented. In particular, the array pattern of the MIMO random array and the statistics of the sidelobe level is reviewed. The expressions for the average peak sidelobe level of a MIMO random array are also developed. It will be shown that the average peak sidelobe level scales logarithmically with the aperture size of the array. In contrast, the number of sensors required in a ULA must scale linearly with the array aperture.

The clutter response of MIMO random arrays is also reviewed. It is seen in this chapter that the clutter ridge becomes narrow due to the high resolution obtained from a MIMO random array. This high resolution however comes at the cost of multiple spurious clutter ridges due to the high sidelobes of the MIMO random array. The clutter rank of the MIMO random array is also presented. It is seen that the clutter rank for the MIMO random array is roughly the same as the clutter rank of a filled ULA of the same aperture size. Since the MIMO random array typically has less degrees of freedom (DOF) available compared to the large filled ULA this means that the MIMO random array will have less DOF available to provide gain for target detection. Finally, the SINR of the MIMO random array is considered, it is seen in this chapter that the high resolution of a MIMO random array allows one to discriminate slow moving targets.

2.1 Signal Model

Consider a MIMO radar system mounted on an aircraft, in which N_r sensors collect echos from N_t transmitters, each transmitter transmits a finite train of N_p-pulse

coherent waveforms with pulse-repetition-interval T_r. It is assumed that the N_t waveforms are orthogonal to each other. The radar operating carrier wavelength is λ, and the airborne platform velocity is v_p, where the velocity vector is assumed aligned with the array axis. The N_r receive sensor positions in wavelength units are given by the sequence $\mathbf{Z}_r = [z_1, z_2, \ldots, z_{N_r}]^T$. Similarly, the positions of the N_t transmitters in wavelength units are given by the sequence $\mathbf{Z}_t = [t_1,\ t_2,\ \ldots\ t_{N_t}]$. Let the aperture size of the receive array and the transmit array be given by Z_r and Z_t respectively, where $Z_r = z_{N_r} - z_1$ and $Z_t = t_{N_t} - t_1$. Then the size of the array is defined by $Z = Z_t + Z_r$. In this dissertation, a MIMO random array is considered where the positions of receive and transmit elements are distributed across the array according to the uniform random variables $U \sim [0, Z_r]$ and $U \sim [0, Z_t]$. An example of a MIMO random array is illustrated in Figure. 2.1.

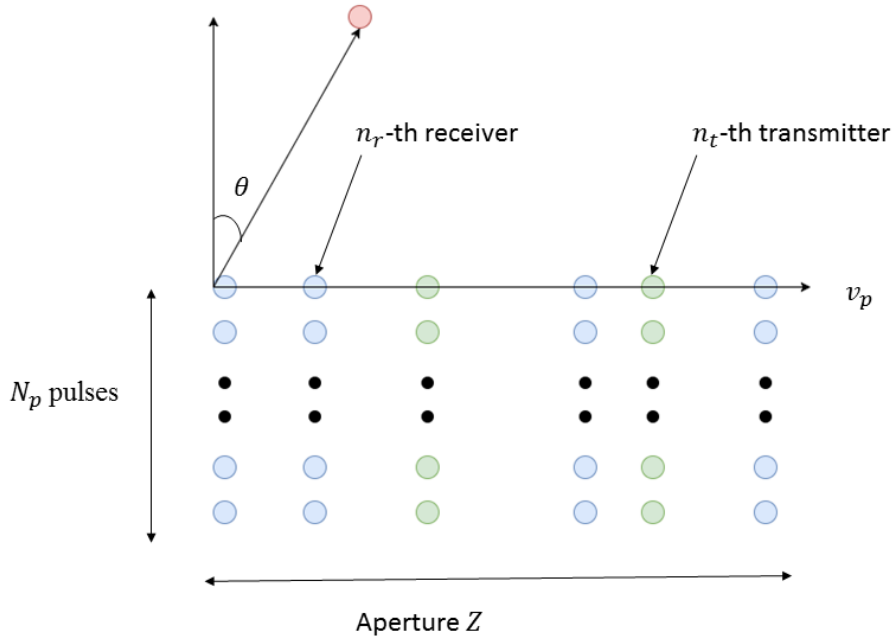

Figure 2.1 Example of a MIMO random array.

Let $u = \sin(\phi)$ denote the spatial frequency associated with the azimuth angle measured with respect to the normal to the array. The $N_r \times 1$ receive steering vector

$\mathbf{c}(u)$, which represents the baseband response of the N_r receive sensors to a target at spatial frequency u, is given by

$$\mathbf{c}(u) = \left[e^{j2\pi z_1 u}, e^{j2\pi z_2 u}, \ldots, e^{j2\pi z_{N_r} u}\right]^T. \tag{2.1}$$

Similarly, the $N_t \times 1$ transmit steering vector $\mathbf{g}(u)$, which represents the response of the target at spatial frequency u, by the N_t transmitters is given by

$$\mathbf{g}(u) = \left[e^{j2\pi t_1 u},\ e^{j2\pi t_2 u},\ \ldots\ e^{j2\pi t_{N_t} u}\right]^T. \tag{2.2}$$

Define the $N_t N_r \times 1$ spatial steering vector $\mathbf{d}(u)$,

$$\mathbf{d}(u) = \mathbf{g}(u) \otimes \mathbf{c}(u) \tag{2.3}$$

where $\otimes$ is the Kronecker product. Similarly, the $N_p \times 1$ temporal steering vector $\mathbf{v}(f)$ for a target with Doppler frequency f is given by

$$\mathbf{v}(f) = \left[1, e^{j2\pi f T_r}, \ldots, e^{j2\pi (N_p - 1) f T_r}\right]^T. \tag{2.4}$$

For notational convenience, let $N = N_r N_t N_p$, then the $N \times 1$ space-time steering vector for a target with spatial frequency u and Doppler f is given by

$$\mathbf{a}(u, f) = \mathbf{v}(f) \otimes \mathbf{d}(u)/\sqrt{N}. \tag{2.5}$$

The term $\sqrt{N}$ appearing in (2.5) is a normalization term and ensures that $\mathbf{a}^H(u, f)\mathbf{a}(u, f) = 1$.

The $N \times 1$ received baseband signal $\mathbf{y}$ at the array from a target at spatial frequency u, Doppler frequency f and with complex amplitude x is given by

$$\mathbf{y} = x\mathbf{a}(u, f) + \mathbf{e}_c + \mathbf{e}_w \tag{2.6}$$

where $\mathbf{e}_c$ is the interference vector of ground clutter and $\mathbf{e}_w$ is a vector of complex white Gaussian noise representing the thermal noise.

In later chapters, optimization algorithms that operate on a discretized grid of points are discussed. To this end, the angle-Doppler map is discretized into $G = \overline{G}^2$ grid points, where $\overline{G}$ is the number of grid points in each of the two domains. Using this grid, the baseband response $\mathbf{y}$ at the array from K targets is given by

$$\mathbf{y} = \mathbf{A}\mathbf{x} + \mathbf{e}_c + \mathbf{e}_w. \tag{2.7}$$

Here, $\mathbf{A} = [\mathbf{a}(u_1, f_1)\, \mathbf{a}(u_1, f_2), \ldots, \mathbf{a}(u_{\overline{G}}, f_{\overline{G}})]$ is a $N \times G$ matrix of steering vectors associated with possible target locations on the angle-Doppler map, $\mathbf{x}$ is a $G \times 1$ vector of target gains that is sparse, in the sense that is has $K \ll G$ nonzero entries. The targets are assumed to comply with the discretized grid.

In this dissertation, the ground clutter and thermal noise are treated as uncorrelated processes, and therefore the $N \times N$ interference covariance matrix is given by

$$\mathbf{R} = \mathbb{E}\left[(\mathbf{e}_c + \mathbf{e}_w)(\mathbf{e}_c + \mathbf{e}_w)^H\right] = \mathbf{R}_c + \mathbf{R}_w. \tag{2.8}$$

Here $\mathbf{R}_w$ is the covariance matrix of the thermal noise given by $\mathbf{R}_w = \sigma^2\mathbf{I}$ where σ^2 is the power of thermal noise. A typical model for the clutter covariance matrix $\mathbf{R}_c$ [**?**] is

$$\mathbf{R}_c = \int_{-1}^{1} s(u_i)\mathbf{a}\left(u_i, \beta u_i\right)\mathbf{a}^H\left(u_i, \beta u_i\right) du \tag{2.9}$$

where s_i is the power of the clutter scatterer at spatial frequency u_i with the normalized Doppler frequency $f(u_i) = \beta u_i$ where $\beta = 4v_p T_r/\lambda$. In this dissertation, it is assumed that $\beta = 1$.

2.2 MIMO Random Arrays

In MIMO random arrays, a low number of receive and transmit antenna elements are placed at random between the end points of a large array. Since the goal is to obtain a thinned array, the average spacing between receive elements is larger than half-wavelength, similarly, the average spacing between transmit elements is larger than half-wavelength. Note that the beam pattern of a filled ULA with aperture Z and uniform illumination is given by

$$\beta_{ULA}(\omega) = \left(\sin(\pi Z\omega) / [Z\sin(\pi\omega)]\right)^2.$$

From this expression, it is easy to see that the main beam is the region $|\omega| \leq 1/Z$, while the sidelobes are $|\omega| > 1/Z$. The number of sidelobes in the visible region $|\omega| < 1$ is $2(Z-2)$. Of interest are sufficiently large values of the aperture Z, such that, for notational convenience, the number of sidelobes may be approximated by $2Z$. For reference, the peak sidelobe of a filled ULA is approximately –13 dB relative to the mainlobe [13].

It has been shown in [29] that a MIMO array with N_t transmitters and N_r receivers behaves like large random array with $N_t N_r$ sensors. The position of the $N_t N_r$ sensors are obtained by convolving the locations of the transmit and receive antennas $\mathbf{Z}_t$ and $\mathbf{Z}_r$. Given an array of $N_t N_r$ elements placed at random over an aperture of Z it has been shown that the shape of the mainbeam $\beta(\omega)$, $|\omega| \leq 1/Z$, follows that of a filled ULA with little variation between instantiations of array elements. Thus with significantly fewer elements, a MIMO random array provides the advantage

of a narrow and stable mainbeam of a filled array. While there is no impact on the mainbeam, random arrays have higher sidelobes than filled arrays illustrated in Figure 2.2.

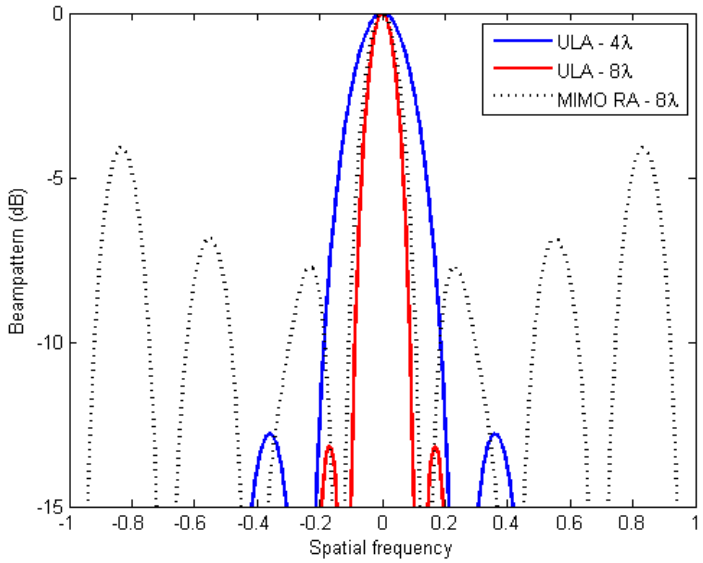

Figure 2.2 Beampattern of a ULA with an array aperture of $Z = 4\lambda$ and $Z = 8\lambda$. The beampattern of a MIMO random array with an array aperture $Z = 8\lambda$ using $N_t = 2$ transmit elements and $N_r = 4$ receive elements is also shown.

By the central limit theorem, for a sufficiently large number of elements $N_t N_r$ and a fixed value ω,

$$\beta(\omega) = |b(\omega)|^2 = |\frac{1}{N_t N_r}\mathbf{d}^H(u-\omega)\mathbf{d}(u)|^2. \tag{2.10}$$

The term $\mathbf{b}(\omega)$ in (2.10) can also be expressed as

$$\begin{aligned}\mathbf{b}(\omega) &= \frac{1}{N_t N_r}\mathbf{d}^H(u-\omega)\mathbf{d}(u) \\ &= \frac{1}{N_t N_r}\sum_{m=1}^{N_t}\sum_{n=1}^{N_r} e^{j2\pi(z_n+t_m)\omega}\end{aligned} \tag{2.11}$$

Examining (2.11), $\mathbf{b}(\omega)$ is the sum of $N_t N_r$ random variables. By the central limit theorem, for sufficiently large $N_t N_r$ and a fixed value ω, the random variable (2.11) is a complex Gaussian random variable with mean

$$\phi(\omega) = \frac{1}{N_t N_r} \sum_{m=1}^{N_t} \sum_{n=1}^{N_r} \mathbb{E}\left[e^{j2\pi(z_n+t_m)\omega}\right] = \mathbb{E}\left[e^{j2\pi(z_n+t_m)\omega}\right]$$

and variance

$$\text{var}\left[|\mathbf{b}(\omega)|^2\right] = \mathbb{E}\left[|\mathbf{b}(\omega)|^2\right] - |\phi(\omega)|^2.$$

It is shown in [32] that in the sidelobe region,

$$\mathbb{E}\left[\text{Re}(b(\omega))^2\right] \approx \mathbb{E}\left[\text{Im}(b(\omega))^2\right] \approx \frac{1}{2N_t N_r}$$

and that, in the sidelobe region $|\omega| > 1/Z$, the term $|\phi(\omega)|^2$ is negligible relative to $\frac{1}{2N_t N_r}$. Therefore, the mean level of the beam pattern sidelobes is

$$\mathbb{E}\left[|b(\omega)|^2\right] = \mathbb{E}\left[\beta(\omega)\right] \approx \frac{1}{N_t N_r}.$$

Thus, the sidelobes of a MIMO random array are dominated by the term $\frac{1}{N_t N_r}$ rather than the sidelobes of the associated filled array. The mainlobes and sidelobes of an 4λ, 8λ ULA and an 8λ random array with $N_t = 2$ transmitters and $N_r = 4$ receive sensors are illustrated in Figure 2.2. Note that the random array achieves with half the number of sensors the same mainlobe as the 8λ ULA. In contrast, the random array sidelobes are higher.

The statistics of the peak sidelobe, $\mu = \max_{|\omega|>1/Z} \beta(\omega)$ are also of great interest. Viewed as a function of ω, the array pattern $\beta(\omega)$ is a stochastic process. In the sidelobe region, the stochastic process is approximately ergodic, meaning that the

statistical averages may be gleaned from averages across the spatial frequency variable ω [32]. Furthermore, values of the stochastic process $\beta(\omega)$ become independent when the values of the spatial frequency ω are separated by a sidelobe or more. As previously discussed, the number of sidelobes is approximately $2Z$. To find the cumulative distribution function (CDF) of the peak sidelobe, let

$$\widetilde{\beta}\left(\omega\right) \triangleq 2N_tN_r\beta\left(\omega\right) = 2N_tN_r\left|b\left(\omega\right)\right|^2$$

and $\widetilde{\mu} \triangleq 2N_tN_r\mu$. Since $b\left(\omega\right) \sim CN\left(0, 1/N_tN_r\right)$, it follows that $\widetilde{\beta}\left(\omega\right)$ is a chi-square random variable with 2 degrees of freedom. It is easy to verify that the CDF of $\widetilde{\beta}\left(\omega\right)$ is given by

$$\Phi_{\widetilde{\beta}}\left(t\right) = 1 - e^{-t/2}. \tag{2.12}$$

It follows that the CDF of the peak sidelobe variable $\widetilde{\mu}$ is

$$\Phi_{\widetilde{\mu}}\left(t\right) = \Pr\{\beta\left(\omega_1\right) \leq t, ..., \beta\left(\omega_{2Z}\right) \leq t\} = \left(\Phi_{\widetilde{\beta}}\left(t\right)\right)^{2Z} \tag{2.13}$$

Using a known relation for non-negative random variables,

$$\mathbb{E}\left[\widetilde{\mu}\right] = \int_0^\infty \left(1 - \Phi_{\widetilde{\mu}}(t)\right) dt \tag{2.14}$$

Substituting (2.12) and (2.13) in (2.14),

$$\mathbb{E}\left[\widetilde{\mu}\right] = \int_0^\infty \left(1 - \left(1 - e^{-t/2}\right)^{2Z}\right) dt. \tag{2.15}$$

The integration in (2.15) is solved in [70], where it is shown

$$\int_0^\infty \left(1 - \left(1 - e^{-t/2}\right)^{2Z}\right) dt = 2\sum_{k=1}^{2Z} \frac{1}{k}. \tag{2.16}$$

For large Z, the sum $\sum_{k=1}^{2Z} \frac{1}{k}$ asymptotically approaches $\ln 2Z + \gamma_E$, where $\gamma_E = 0.577$ is Euler's constant [70]. Since, $\ln(2Z) \gg \gamma_E$, the following approximation is made $\sum_{k=1}^{2Z} \frac{1}{k} \approx \ln(2Z)$. Substituting this back into (2.15), $E[\widetilde{\mu}] = 2 \ln 2Z$. Finally, recalling that the peak sidelobe μ is related to the random variable $\widetilde{\mu}$ as $\mu = \widetilde{\mu}/2N_tN_r$, the mean peak sidelobe is given by

$$\mathbb{E}[\mu] = \frac{\ln(2Z)}{N_tN_r}$$

Figure 2.3 shows a beampattern of an 8λ MIMO random array. The peak and average sidelobe levels are also shown. It is observed that the mean peak sidelobe is larger than the mean sidelobe by the factor $\ln(2Z)$. Also, to maintain a fixed mean peak sidelobe level, the product N_tN_r has to scale with the logarithm of the aperture length. This is contrast with a filled ULA in which the number of elements scales with Z. The beampattern of a MIMO random array along with the average sidelobe and average peak sidelobe level is illustrated in Figure 2.3.

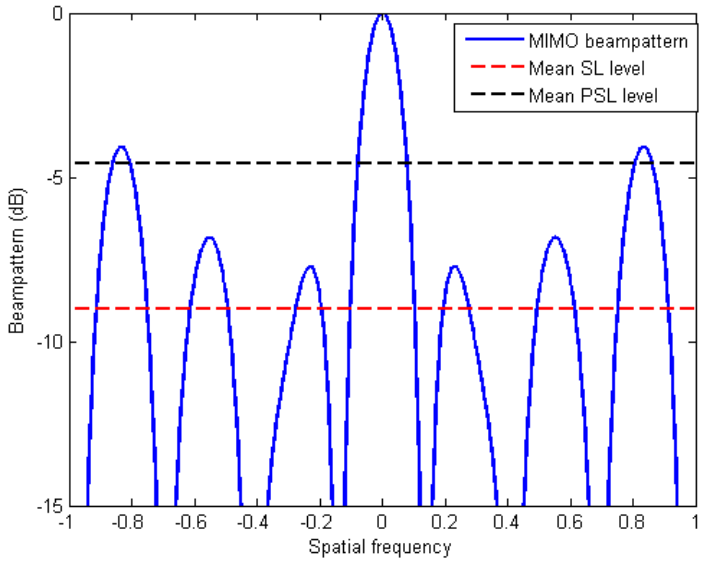

Figure 2.3 Beampattern of a MIMO random array with an array aperture $Z = 8\lambda$ using $N_t = 2$ transmit elements and $N_r = 4$ receive elements. The average sidelobe level and the average peak sidelobe level is also displayed.

Another point of view that demonstrates that the number of necessary elements in a random array scales with $\ln Z$ rather than Z, is to compute the number of elements for which the peak sidelobe μ is lower than a level η, with probability α, $\alpha = \Pr\{\mu \leq \eta\} = \Phi_\mu(\eta)$. The CDF of the peak sidelobe $\Phi_\mu(t)$ can be computed from (2.13) and (2.12). Recalling the relation $\mu = \widetilde{\mu}/2N_tN_r$,

$$\alpha = \Phi_{\widetilde{\mu}}(2N_tN_r\eta) = \left(1 - e^{-N_tN_r\eta}\right)^{2Z} \tag{2.17}$$

Taking ln of both sides, and noting that the expected result is such that $N_tN_r\eta \gg 1$, the ln function is approximated with the first term in its Taylor expansion

$$\ln\left(1 - e^{-N_tN_r\eta}\right) \approx -e^{-N_tN_r\eta} \tag{2.18}$$

Using (2.18) and after a little algebra, obtain

$$N_tN_r = \frac{1}{\eta}\left(\ln 2Z - \ln\ln\alpha^{-1}\right)$$

which links between the number of elements and confidence level that the sidelobes do not exceed a set value. A similar result without proof has been presented in [34].

2.3 Clutter Response

STAP relies on the fact that the rank of the clutter covariance matrix $\mathbf{R}_c$ (often referred to as *clutter rank*) is much lower than the dimensionality of the signal space. As a result, whitening of the clutter interference does not result in significant loss of target SNR. In a filled ULA, the clutter map (defined as $\mathbf{a}^H(u,v)\mathbf{R}_c\mathbf{a}(u,v)$, with u and v sweeping through their domains $|u| < 1$, $|v| < 1$), forms a diagonal ridge above the uv plane. The width of the ridge along the spatial frequency u axis equals the beamwidth of the array. Thus the clutter ridge of a random array is expected to be narrower than the clutter ridge of a filled ULA with the same number of elements. This is illustrated in Figure 2.4. The panel on the left of Figure 2.4 shows the clutter

map of a ULA with $N_r = 8$ elements, while the panel on the right shows the clutter map of a random array of the same number of receive elements (8) spread over 8λ (rather than the 4λ ULA aperture). It is noticed that the clutter ridge of the random array is narrower, which leads to a lower MDV. Note that the clutter map of the sparse array also exhibits multiple, spurious clutter ridges due to higher sidelobes of the beampattern.

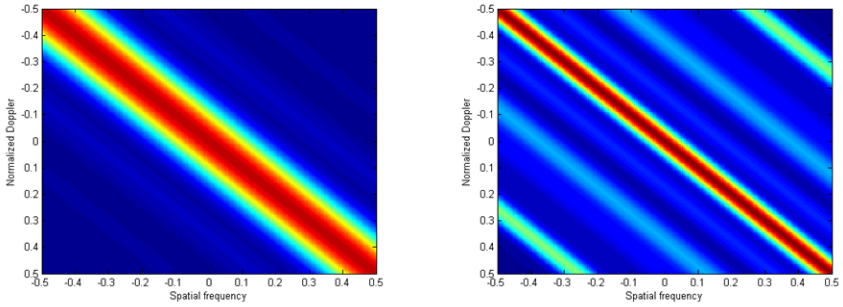

Figure 2.4 (Left figure): Clutter map using a ULA with $N_r = 8$ elements, $N_p = 16$ pulses, and $\beta = 1$. (Right figure): Clutter map using a random array with $N_r = 8$ elements, $N_p = 16$ pulses, and $\beta = 1$. The elements of the sparse random array are spread across an array of size 8λ.

The clutter map of a MIMO random array is illustrated in Figure 2.5, the number of transmitter is $N_t = 2$ and the number of receivers is $N_r = 4$, the aperture size of the array is given by $Z = Z_{tx} + Z_{rx} = 8\lambda$. Comparing the clutter map of the random array to the MIMO random array, it is noticed that the width of the clutter ridge has a similar width. This suggests that by using a MIMO random array one can reduce the number of sensors compared to that of the random array and obtain similar performance in terms of the resolution.

Next, a comparison between the ULA, random array, and a MIMO random array from the point of view of the clutter rank is now presented. The rank of the clutter is a measure of the degrees of freedom (DOF) captured by the clutter, and thus lost in the process of suppressing the clutter. To avoid confusion, let $\mathbf{R}_c$ represent

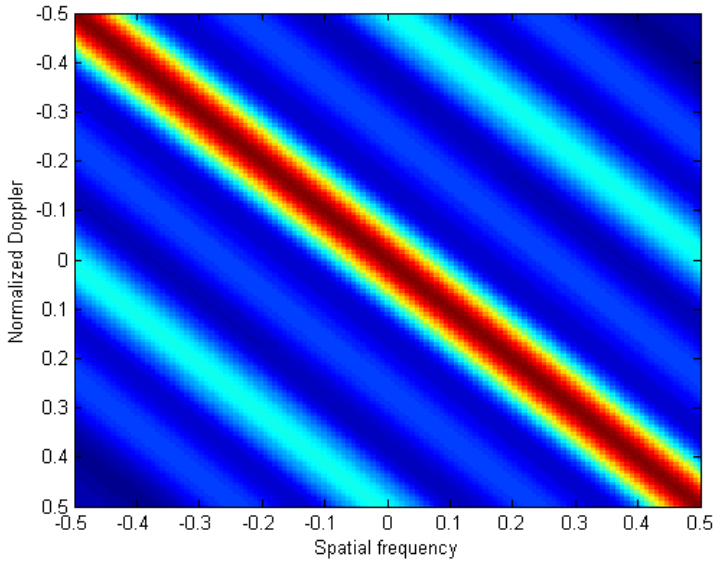

Figure 2.5 Clutter map using a MIMO random array with $N_r = 4$ elements, $N_t = 2$ transmitters, $P = 16$ pulses, and $\beta = 1$. The MIMO random array has an aperture size of $Z = 8\lambda$.

the clutter covariance matrix for the ULA, and $\overline{\mathbf{R}}_c$ represent the clutter covariance matrix for the random array. From Brennan's rule [71], the clutter rank of a ULA is given by the

$$r_c = \text{rank}(\mathbf{R}_c) = N_a + (N_p - 1)\beta. \tag{2.19}$$

Now, given a or MIMO random array with aperture size Z, let N_a^{full} represent the number of sensors required to fill the array with a ULA configuration. Then, from [9], the clutter rank of a random array is

$$\overline{r}_c \approx N_a^{full} + (N_p - 1)\beta. \tag{2.20}$$

It is noticed that the clutter rank of a MIMO random array and the random array depends on the aperture size Z, which controls the value of N_{full}. Figure 2.5 displays the clutter rank of four different array configurations: ULA's with 8 and 16

elements, a random array with 8 elements spread over 8λ, and a MIMO random array with $N_t = 2$ transmitters and $N_r = 4$ receivers with array aperture 8λ. From the figure it is clear that the ULA with $N = 8$ has the smallest rank, while the ULA with $N = 16$, the random array, and the MIMO random array have similar clutter rank when they have an aperture of 8λ. This means the MIMO random array and the random array will require the same number of DOF to suppress the clutter as a large ULA. Hence, the number of DOF left for target gain will generally be lower than the ULA. This discussion points to a trade-off between resolution on one hand, and signal to interference and noise ratio (SINR) on the other hand.

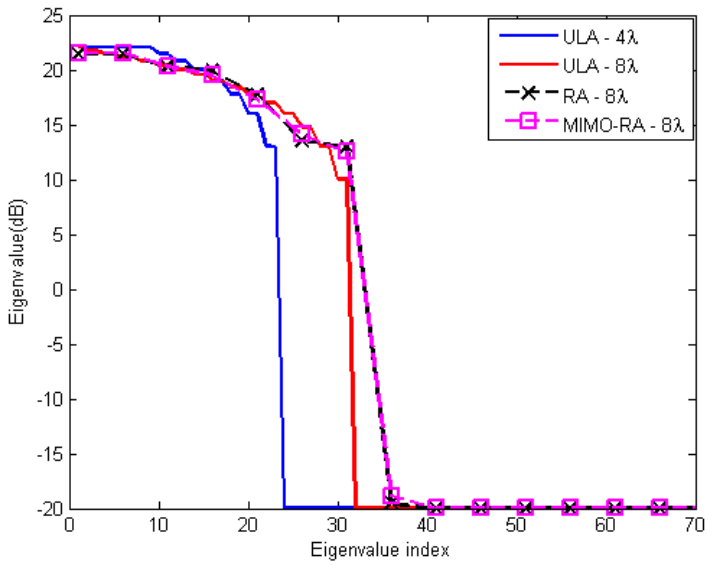

Figure 2.6 Eigenspectra of the clutter and noise covariance matrix for a ULA with $N_r = 8$ elements and $N_r = 16$ elements, random array $N_r = 8$ elements and a MIMO random array with $N_t = 2$ and $N_r = 4$, the aperture size of the random array and the MIMO random array is $Z = 8\lambda$. The number of pulses N_p for each array configuration is $N_p = 16$.

To further illustrate the performance differences between the ULA, random array and the MIMO random array in Figure 2.7 is shown the SINR for various array configurations. The array configurations considered are the following: ULA's with 8 and 16 elements, a random array with 8 elements spread over 8λ, and a MIMO

random array with $N_t = 2$ transmitters and $N_r = 4$ receivers with array aperture 8λ. The SINR is given by $\mathbf{a}(u, f)\mathbf{R}^{-1}\mathbf{a}(u, f)$. For the figure, the spatial frequency is fixed and set to $u = 0$. From the figure, it is seen that the small ULA with 8 elements has a lowest SINR than the other array configurations close to $f = 0$ where the clutter scatterer is located. On the other hand, the remaining array configurations show nearly identical SINR responses near the clutter scatterer. The width of the SINR response near the clutter scatterer gives an indication of how low the target's Doppler can be while still being detected. This corresponds to how slow a target can move but still be detected which is often referred to as the minimum detectable velocity (MDV). The wider SINR response of the small ULA points to a larger MDV whereas the smaller width of the remaining array configurations points to a smaller MDV.

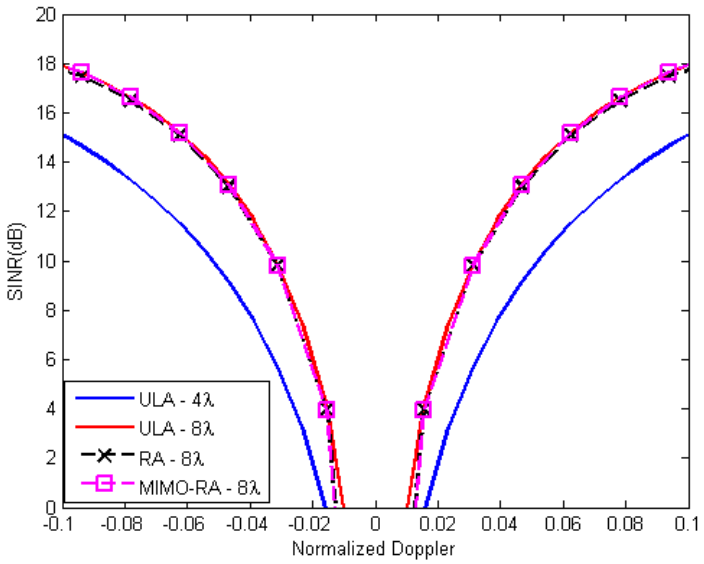

Figure 2.7 SINR vs Doppler for four array configurations near the clutter scatterer. Arrays used are: ULA of size 4λ, ULA of size 8λ, random array with $N = 8$ elements of size 8λ, and a MIMO random array with $M = 4$ transmit elements, $N = 4$ receive elements of array size 8λ. For all arrays $\beta = 1$ and $P = 16$.

In Figure 2.8, the SINR response is shown for large Doppler for four array configurations. Again, the array configurations considered are the following: ULA's with 8 and 16 elements, a random array with 8 elements spread over 8λ, and a MIMO

random array with $N_t = 2$ transmitters and $N_r = 4$ receivers with array aperture 8λ. From the figure, for most Dopplers, a negligible loss in SINR is observed for the MIMO and random array compared to the ULA configurations. The SINR of the MIMO random array hovers around 16 to 18 dB whereas the random array attains an SINR of about 18 dB. This 2-4 dB loss occurs because the fraction of DOFs available to the and MIMO random array is less than that of the ULAs.

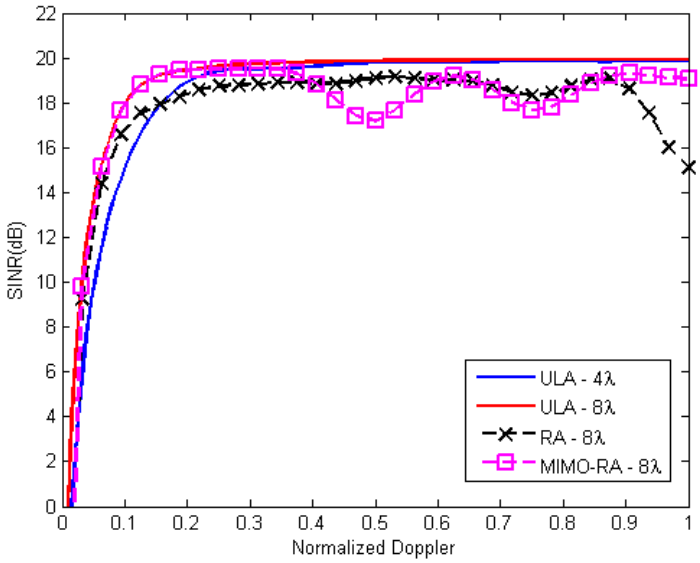

Figure 2.8 SINR vs Doppler for four array configurations far from the clutter scatterer. Arrays used are: ULA of size 4λ, ULA of size 8λ, random array with $N = 8$ elements of size 8λ, and a MIMO random array with $M = 4$ transmit elements, $N = 4$ receive elements of array size 8λ. For all arrays $\beta = 1$ and $P = 16$.

2.4 Concluding Remarks

In this chapter, the signal model that will be used throughout this dissertation is introduced. In addition, several properties of the MIMO random array has been analyzed. In particular, the expressions for the average sidelobe level and the average peak sidelobe level were derived. It was shown that the average sidelobe level is inversely proportional to the product $N_t N_r$ where N_r is the number of receive sensors and N_t is the number of transmitters in the array. The average peakside lobe level

was shown to be larger than the average sidelobe level by a factor of $\ln(2Z)$ where Z is the array aperture length in wavelength units. This is in contrast with a ULA where the number of receive sensors scale linearly with the aperture.

The clutter response of a MIMO random array was also presented in this chapter. It was seen that the high resolution of the MIMO random array causes the clutter ridge to become narrow at the cost of multiple spurious clutter ridges due to the high sidelobes of the MIMO random array. In addition, the clutter rank of the MIMO random array was analyzed. It was seen that the clutter rank of a MIMO random array is similar to that of a filled array of the same size. Since the MIMO random array has fewer DOF available to it compared to a large filled ULA, it must spend a larger portion of its available DOF to cancel the clutter. This means less DOFs are available to provide gain for target detection which points to a trade off between the resolution of the radar and the SINR. Although the MIMO random array experiences a small loss in SINR, the high resolution of the array is capable of detecting slow moving targets and has a low MDV.

CHAPTER 3

SPARSITY BASED GMTI RADAR

The goal of GMTI radar is to determine the number of targets present and their positions on the angle-Doppler map. In this chapter, two approaches to solving this problem are discussed. The first approach is to divide the angle-Doppler map into G resolution cells then perform G detection tests, one for each of the G grid points, for the presence of a target. The number of targets is determined by counting the number of cells that pass the detection test, and the positions of the targets depend on the cells that pass the test, this algorithm is referred to as beamforming.

The second approach motivated by advances in compressive sensing (CS), relies on the sparsity of the targets and solves an optimization problem to determine a small set of angle-Doppler resolution cells that may contain targets. The resolution cells obtained from solving the optimization problem are then tested for the presence of a target. The number of targets is determined by counting the number of cells that pass the detection test, and the positions of the targets depend on the cells that pass the test. This approach inspired by [55], is shown to cope with the high sidelobes of a MIMO random array. This allows one to enjoy the high resolution of the MIMO random array without suffering a significant increase in false alarms due to the high sidelobes.

3.1 Adaptive Beamforming

As previously stated, one common approach to solving the detection problem is to divide the angle-Doppler map into G resolution cells and perform G detection tests, one for each of the G grid points. The number of targets is determined by counting the number of cells that pass the detection test, and the locations of the targets are determined by the cells that pass the test. The binary hypothesis test for any of the

resolution cells based on the model (2.6) is given by

$$H_0 : x = 0$$

$$H_1 : x \neq 0.$$

To recap, the problem of testing a STAP resolution cell for the presence of a target of unknown amplitude observed in the presence of Gaussian colored noise with unknown covariance matrix, when secondary data is available for estimating the covariance matrix is posed. This is a classic GLRT problem that has been solved in [72], where it is shown that the test statistic has a CFAR property in the sense that it is independent of the covariance matrix of the interference and noise. As shown in [72], application of the GLRT procedure when the unknowns are the amplitude x and the covariance matrix $\mathbf{R}$, results in a test statistic that, under both hypotheses, is dependent on the primary as well as the secondary data. A simpler approach is suggested in [73], where the likelihood of the observation is maximized only over the unknown amplitude (separately for each hypothesis). In this approach, the covariance matrix is assumed known through the derivation of the test statistic, but is substituted with the sample covariance matrix of the secondary data in the final expression of the test statistic. While this procedure is ad-hoc, it is argued in [73] that the resulting test statistic differs from GLRT statistic in [72] only by a term that vanishes when the set of secondary data is large. The test for deciding H_1 for a resolution cell defined by the steering vector $\mathbf{a}$ is given by [73]

$$T = \frac{|\mathbf{a}^H \widehat{\mathbf{R}}^{-1} \mathbf{y}|^2}{\mathbf{a}^H \widehat{\mathbf{R}}^{-1} \mathbf{a}} \geq \gamma. \tag{3.1}$$

It is noted that the test statistic is essentially a beamfomer $\mathbf{a}^H$ applied to whitened observations $\widehat{\mathbf{R}}^{-1}\mathbf{y}$ and normalized by the interference and noise power $\mathbf{a}^H \widehat{\mathbf{R}}^{-1} \mathbf{a}$, hence this approach if referred as adaptive beamforming (ABF).

3.2 MP-STAP

In this section, a different approach from the ABF is proposed, one that relies on the sparsity of targets. Detection by beamforming is agnostic to the possible presence of multiple targets. In contrast, the model (2.7) accounts for multiple targets. As explained in Chapter 2, the number of rows of $\mathbf{A}$, N, is much smaller than the number of columns G. The problem of recovering $\mathbf{x}$ given $\mathbf{y}$ and $\mathbf{A}$ is then underdetermined, and hence does not have a unique solution. However, the following problem does accept a unique solution,

$$\min_{\mathbf{x}} \|\mathbf{y} - \mathbf{A}\mathbf{x}\|_2^2 \text{ subject to } \|\mathbf{x}\|_0 \leq K \tag{3.2}$$

where $\|\mathbf{x}\|_0$ denotes the number of nonzero elements of $\mathbf{x}$. In radar, clutter contributions are typically much stronger than the unknown targets and, if not suppressed, may severely interfere with target detection. A whitening operation is applied to the observed data and to the measurement matrix $\mathbf{A}$. Specifically, let $\mathbf{z} = \widehat{\mathbf{R}}^{-1/2}\mathbf{y}$ and $\mathbf{B} = \widehat{\mathbf{R}}^{-1/2}\mathbf{A}$, then optimization (3.2) becomes

$$\min_{\mathbf{x}} \|\mathbf{z} - \mathbf{B}\mathbf{x}\|_2^2 \text{ subject to } \|\mathbf{x}\|_0 \leq K. \tag{3.3}$$

Unfortunately, to solve (3.3) one requires the knowledge of number of targets K, which of course is unknown apriori. Although the number of targets is K is unknown, it is assumed that an upper bound on the number of targets $\overline{K}$ is known as in [55]. To develop a radar that exploits sparsity, a two stage detection algorithm that can approximate the solution to (3.3) utilizing the upper bound on the number of targets $\overline{K}$ referred to as MP-STAP is presented. In the first phase, $\overline{K}$ candidate targets are localized using MP; in the second phase, the $\overline{K}$ localized targets are tested for the presence of a target. If one or more of the localized targets do not pass a detection test, the upper bound on the number of targets is decreased by one and the algorithm is rerun with the new value of $\overline{K}$. This process continues until all $\overline{K}$ targets pass the

detection test or when $\overline{K} = 0$. A block diagram of the MP-STAP algorithm is shown in Figure 3.1.

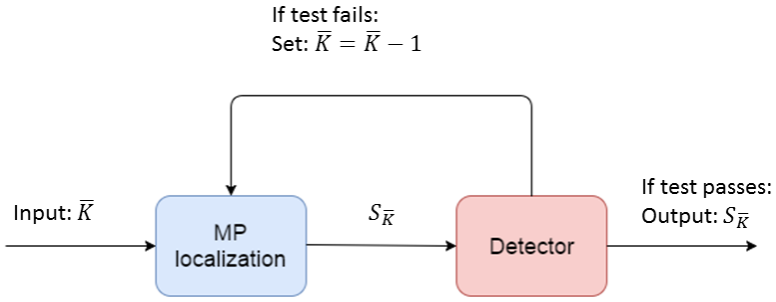

Figure 3.1 Block diagram of the MP-STAP algorithm

3.2.1 Stage 1: Target Localization

The inputs to MP-STAP are whitened data $\mathbf{z} = \widehat{\mathbf{R}}^{-1/2}\mathbf{y}$, whitened steering vectors $\mathbf{b}_j = \widehat{\mathbf{R}}^{-1/2}\mathbf{a}_j$, $j = 1, ..., G$, and the upper bound on the number of targets $\overline{K}$. The first target is localized by the index m_1 of the vector $\mathbf{b}_j$ that has the largest data projection,

$$m_1 = \arg\max_j \frac{|\mathbf{b}_j^H \mathbf{z}|^2}{\mathbf{b}_j^H \mathbf{b}_j} \tag{3.4}$$

for $j = 1, ..., G$. The index m_1 localizes the target in the angle-Doppler domains.

Next, the localization of the k-th candidate target is described, given that $k-1$ targets have already been localized. The steering vectors are processed to cancel the contributions of previously detected targets. Let a matrix $\mathbf{B}$ be formed with the columns $\mathbf{b}_j$. Let S_{k-1} be the set of indices of columns of $\mathbf{B}$ associated with localized targets, and let $\mathbf{B}_{S_{k-1}}$ be the matrix formed by the columns indexed by S_{k-1}. The projection matrix orthogonal to the detected targets is given by $\mathbf{P}^{\perp}_{\mathbf{B}_{S_{k-1}}} = \mathbf{I} - \mathbf{B}_{S_{k-1}} \left(\mathbf{B}^H_{S_{k-1}} \mathbf{B}_{S_{k-1}} \right)^{-1} \mathbf{B}_{S_{k-1}}$. The steering vectors orthogonal to the detected targets are formed as follows: $\mathbf{w}_j = \mathbf{P}^{\perp}_{\mathbf{B}_{S_{k-1}}} \mathbf{b}_j$, for all $j \notin S_{k-1}$. The k-th target is

localized according to

$$m_k = \arg\max_j \frac{|\mathbf{w}_j^H \mathbf{z}|^2}{\mathbf{w}_j^H \mathbf{w}_j} \tag{3.5}$$

This process continues until $\overline{K}$ targets have been localized.

3.2.2 Stage 2: Detection

The detector used to test the $\overline{K}$ targets obtained in the first stage is now detailed. Let $S_{\overline{K}}$ be a set of indicies that correspond to the resolution cells obtained in Stage 1. The signal model is then given by the expression

$$\mathbf{z} = \mathbf{B}_{S_k} \mathbf{x}_{S_k} + \mathbf{n}. \tag{3.6}$$

Let m_k be the k-th element in the set $S_{\overline{K}}$ and the resolution cell that is under test. From [55], the test statistic used for detection is given by

$$T = \frac{|\hat{\mathbf{x}}_{m_k}|^2}{b_k \hat{\sigma}^2} \geq \gamma. \tag{3.7}$$

Here, $\hat{\mathbf{x}}_{m_k}$ is defined as

$$\hat{\mathbf{x}}_{m_k} = \mathbf{u}_k^H \mathbf{B}_{S_k}^{\dagger} \mathbf{z},$$

$\hat{\sigma}^2$ is defined as

$$\hat{\sigma}^2 = \|\mathbf{P}^{\perp}_{\mathbf{B}_{S_{\overline{K}}}} \mathbf{z}\|_2^2 / (N - \overline{K}),$$

and b_k is defined as

$$b_k = \mathbf{u}_k^H \left(\mathbf{B}_{S_k}^H \mathbf{B}_{S_k}\right)^{-1} \mathbf{u}_k$$

where $\mathbf{u}_k$ is a $\overline{K} \times 1$ vector where the k-th entry is equal to 1 and the remaining entries are equal to zero. The detection test is performed for $k = 1, \ldots, \overline{K}$. If all $\overline{K}$ targets pass the detection test, $S_{\overline{K}}$ is declared the set of targets, otherwise, $\overline{K}$ is decremented by one and the MP-STAP is reran with the new value of $\overline{K}$. The pseudocode for the MP-STAP algorithm is listed in Algorithm 1.

Algorithm 1 MP-STAP

1: **Input**: $\mathbf{y}, \mathbf{A}, \hat{\mathbf{R}}, \overline{K}, \gamma$.

2: **Initialize**: $S_0 = \emptyset$, $\mathbf{r} = \hat{\mathbf{R}}^{-1/2}\mathbf{y}$, $\mathbf{B} = \hat{\mathbf{R}}^{-1/2}\mathbf{A}$, $\mathbf{W} = \mathbf{B}$, $k = 1$.

3: **Find**: Search for the index l that maximizes the metric $\max_j \ |\mathbf{w}_j^H \mathbf{r}|^2 / \mathbf{w}_j^H \mathbf{w}_j$.

4: **Update set of targets**: $S_k = S_{k-1} \bigcup l$.

5: **Generate**: $\mathbf{P}^{\perp}_{\mathbf{B}_{S_k}} = \mathbf{I} - \mathbf{B}_{S_k} \left(\mathbf{B}_{S_k}^H \mathbf{B}_{S_k} \right)^{-1} \mathbf{B}_{S_k}^H$.

6: **Remove found targets**: $\mathbf{W} = \mathbf{P}^{\perp}_{\mathbf{B}_{S_k}} \mathbf{B}$.

7: **Renormalize**: **If** $\|\mathbf{w}_i\|_2 = 0$, set $\mathbf{w}_i = \mathbf{0}$.

8: **If** $k < \overline{K}$ Return to step 3, otherwise, continue to step 9

9: **Check**: **If** $T \geq \gamma$ for all $s_i \in S_k$ Terminate. Otherwise, set $\overline{K} = \overline{K} - 1$ and return to step 2.

3.3 MBMP-STAP

The MP-STAP algorithm localizes the first target according to (3.4), namely, finds the column of the whitened measurement matrix with the largest projection on the whitened data $\mathbf{z}$. A false alarm (localizing the target in the wrong resolution cell) increases the chance of further false alarms downstream, since according to (3.5), localizing subsequent candidate targets depends on the location of the first target (3.4). A more robust approach is to hedge bets by finding multiple candidates for the location of the first target. Each such candidate target serves as seed to the localization and detection of subsequent targets. When the process is completed, a

metric is used to select the set of targets that provides the best fit to the data. This algorithm, which generalizes MP-STAP is referred to as MBMP-STAP.

Some notation is introduced that facilitates the presentation of MBMP-STAP. A localization solution is referred to as a branch. The set $D = \{d_1, d_2, ..., d_k\}$ contains the number of branches per target. A path is a sequence of branches specified by their index numbers. For example the path $(i_1, i_2, ..., i_k)$, $1 \leq i_1 \leq d_1, ..., 1 \leq i_k \leq d_k$. A localization solution $1 \leq m_k^{(i_1,i_2,...,i_k)} \leq G$, where G is the number of resolution cells (see (2.7)), consists of a path and the index number of the resolution cell. The set $S_k^{(i_1,...,i_k)} = \left\{m_1^{(i_1)}, m_2^{(i_1,i_2)}, ..., m_k^{(i_1,...,i_k)}\right\}$ contains the localization solution associated with path $(i_1, i_2, ..., i_k)$. For k candidate targets, MBMP-STAP maintains $d_1 \times d_2 \times ... \times d_k$ such sets. The matrix $\mathbf{B}_{S_k}$ was defined to consist of the whitened steering vectors $\mathbf{b}_j$ indexed by S_k.

3.3.1 Stage 1: Target Localization

The inputs to MBMP-STAP are the whitened measurement vector $\mathbf{z} = \widehat{\mathbf{R}}^{-1/2}\mathbf{y}$, whitened steering vectors $\mathbf{b}_j = \widehat{\mathbf{R}}^{-1/2}\mathbf{a}_j$, for $j = 1, ..., G$, the upper bound on the number of targets $\overline{K}$, and a set of positive integers $D = \{d_1, d_2, \ldots, d_{\overline{K}}\}$. To localize the candidates for the first target, the algorithm finds the d_1 indices $m_1^{(1)}, m_1^{(2)}, \ldots, m_1^{(d_1)}$ that produce the d_1 largest projections of steering vectors $\mathbf{b}_j$ on the data $\mathbf{z}$. Specifically, the resolution cell index that localizes the first branch of the first target is found from

$$m_1^{(1)} = \arg\max_j \frac{|\mathbf{b}_j^H \mathbf{z}|^2}{\mathbf{b}_j^H \mathbf{b}_j} \tag{3.8}$$

The i-th branch of the first target, $1 \leq i \leq d_1$, is found from

$$m_1^{(i)} = \arg\max_{j \notin \{m_1,...,m_{i-1}\}} \frac{|\mathbf{b}_j^H \mathbf{z}|^2}{\mathbf{b}_j^H \mathbf{b}_j} \tag{3.9}$$

To generate the d_2 branches associated with the second target, define the modified steering vectors $\mathbf{w}_j^{(i)} = \mathbf{P}_{\mathbf{B}_{m_1^{(i)}}}^{\perp} \mathbf{b}_j$, for $1 \leq i \leq d_1$. The resolution cell index associated with the first branch of the second target is given by

$$m_2^{(1,1)} = \arg\max_j \frac{|\mathbf{w}_j^{(1)H}\mathbf{z}|^2}{\mathbf{w}_j^{(1)H}\mathbf{w}_j^{(1)}} \tag{3.10}$$

whereas the index of branch i_2, $1 \leq i_2 \leq d_2$ of the second target, given the path (i_1, i_2),

$$m_2^{(i_1,i_2)} = \arg\max_{j \notin \{m_1,\ldots,m_{i_2-1}\}} \frac{|\mathbf{w}_j^{(i_1)H}\mathbf{z}|^2}{\mathbf{w}_j^{(i_1)H}\mathbf{w}_j^{(i_1)}} \tag{3.11}$$

Generalizing to k targets and the path $(i_1, i_2, ..., i_k)$, define the vector $\mathbf{w}_j^{(i_1,\ldots,i_k)} = \mathbf{P}_{\mathbf{B}_{S_{k-1}^{(i_1,\ldots,i_{k-1})}}}^{\perp} \mathbf{b}_j$. The index associated with the k-th target is given by

$$m_k^{(i_1,\ldots,i_k)} = \arg\max_{j \notin \{m_1,\ldots,m_{i_k-1}\}} \frac{\left|\mathbf{w}_j^{(i_1,\ldots,i_{k-1})H}\mathbf{z}\right|^2}{\mathbf{w}_j^{(i_1,\ldots,i_{k-1})H}\mathbf{w}_j^{(i_1,\ldots,i_{k-1})}}. \tag{3.12}$$

An example of MBMP-STAP with $D = \{2, 2, 1, \ldots\}$ is illustrated in Figure 3.2.

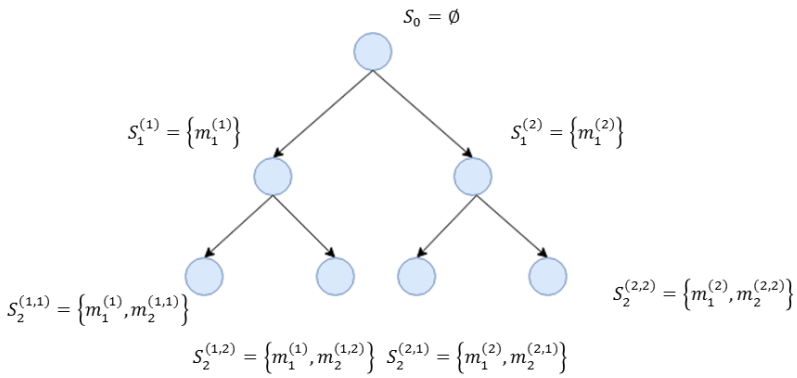

Figure 3.2 Graph of MBMP algorithm for a branch vector $\mathbf{d} = [2,\ 2]^T$.

Intuitively, the MBMP-STAP algorithm generalizes the MP-STAP by allowing the consideration of resolution cells that do not maximize the metric in (3.5). By allowing the algorithm the freedom to test more resolution cells the probability of false

alarm associated with the algorithm localizing an incorrect resolution cell decreases.
‘

3.3.2 Stage 2: Detection

The MBMP localization processing yielded $d_1 \times \ldots \times d_{\overline{K}}$ target sets that contain $\overline{K}$ targets. The residual along the path $(i_1, i_2, ..., i_k)$ is computed from

$$R^{\left(i_1,\ldots,i_{\overline{K}}\right)} = \left\| \mathbf{P}^{\perp}_{\mathbf{B}_{S^{\left(i_1,\ldots,i_{\overline{K}}\right)}_{\overline{K}}}} \mathbf{z} \right\|_2^2 .$$

The path that yields the lowest residual is given by

$$(i_1, i_2, ..., i_{\overline{K}}) = \arg \min_{\left(j_1,\ldots,j_{\overline{K}}\right)} R^{\left(j_1,\ldots,j_{\overline{K}}\right)}.$$

The set $S_{\overline{K}}$ is then set to $S_{\overline{K}} = i_1, i_2, ..., i_{\overline{K}}$. The targets in the set $S_{\overline{K}}$ is then tested for the presence of a target using (3.7) for $k = 1, \ldots, \overline{K}$. If all $\overline{K}$ targets pass the detection test $S_{\overline{K}}$ is declared the set of targets, otherwise, $\overline{K}$ is decremented by one and the MBMP-STAP is reran with the new value of $\overline{K}$.

3.4 Numerical Results

In this section, numerical results on the MP-STAP and MBMP-STAP algorithms are presented and compared to against the ABF. Unless stated otherwise, in figures presented in this section, the aperture of the MIMO random arrays is 8λ ($Z = 8$, where recall that Z is expressed in units of wavelength). The number of transmit elements in the random array is $N_t = 2$, and the number receive elements is given by $N_r = 4$. The number of coherent pulses used by all arrays is $N_p = 16$. The SNR, defined as $|x|^2/\sigma^2$ is set to SNR = 18 dB unless stated otherwise, the clutter-to-noise ratio (CNR) is set to 30 dB. The number of training samples used to estimate the covariance matrix for the random array is $L = 2N$. The number of resolution cells

on the angle-Doppler map is given by $G = (2Z + 1)^2 = 289$. A random realization of a MIMO random array is generated and remains fixed throughout the Monte Carlo simulations. Let S_t be the true set of resolution cells that contain targets, and let $\hat{S}$ be the set of resolution cells found by a detector to have targets. A false alarm event occurs is $\hat{S} \setminus S_t \neq \emptyset$, and a detection event occurs if $\hat{S} \bigcap S_t \neq \emptyset$.

In Figure 3.3 are shown the ROC curves for a single target in field of view for the ABF and the MP-STAP algorithms. The target in the field of view is a slowly moving target. The target is placed at $(u = 0, f = 1/N_p)$, near the clutter ridge in the angle-Doppler map. From the figure, it is seen that the ABF experiences a high false alarm rate due to the high sidelobes of the MIMO random array. In particular, to obtain a probability of detection of about 0.9, the ABF must tolerate an unacceptable probability of false alarm of about 0.1. On the other hand, MP-STAP performs well even in the presence of high sidelobes, for the MP-STAP algorithm to obtain a probability of detection of about 0.9 the MP-CFAR must tolerate a reasonable probability of false alarm of about 10^{-3}.

In Figure 3.4 is shown the ROC curves for two targets in field of view for the ABF and the MP-STAP algorithms. Two targets with spatial frequency $u = 0$ are placed on the angle-Doppler map. Both targets are slowly moving, one target has a Doppler $1/N_p$ while the other has a Doppler of $-1/N_p$. Not surprisingly, the ABF fails to obtain acceptable performance and still experiences a high false alarm rate due the high sidelobes of the MIMO random array. The ROC curve of the MP-STAP moves slightly to the right compared to the ROC of MP-STAP in Figure3.3. This slight degradation in performance occurs because the probability that MP-STAP incorrectly localizes a target slightly increases as the number of targets increase. MBMP-STAP shows an improvement in performance compared to MP-STAP. Since MBMP-STAP has additional target sets available for localization estimation the probability that MBMP-STAP incorrectly localizes a target is less than or at worst, equal to the

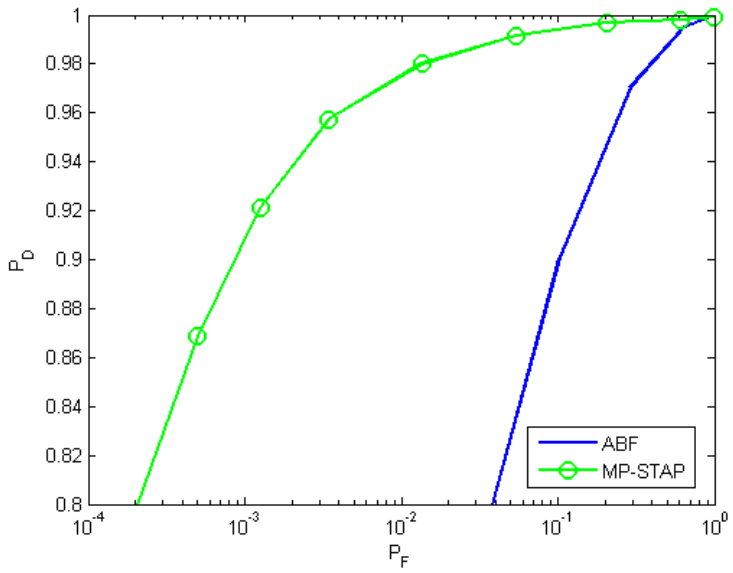

Figure 3.3 ROC curve for the ABF and MP-STAP with a $Z = 8\lambda$ MIMO random array with $N_t = 2$ and $N_r = 4$. The target has the angle-Doppler pair $(u = 0, f = 1/N_p)$. Parameters used: $K = 1$, SNR=18dB, CNR = 30dB

probability that MP-STAP incorrectly localizes a target and hence an improvement is observed.

In Figure 3.5 is shown the probability of detection vs the product $N_t N_r$ for two targets in the field of view for the MP-STAP and MBMP-STAP algorithms. Two targets with spatial frequency $u = 0$ are placed on the angle-Doppler map. Both targets are slowly moving, one target has a Doppler $1/N_p$ while the other has a Doppler of $-1/N_p$. The threshold for both MP-STAP and MBMP-STAP is set to $\gamma = 16$, which is the value of γ that achieves a detection probability of about 0.92 for the MBMP-STAP algorithm in Figure 3.4. To generate the figure, the result of 10^3 Monte Carlo simulations are averaged, for every Monte Carlo simulation, a new realization of a MIMO random array is drawn. From the figure, is it seen that the probability of detection for MBMP-STAP is higher than the MP-STAP for all values of $N_t N_r$. The increase in the probability of detection for MBMP-STAP can be attributed to the multiple localization solutions that is obtained by MBMP-STAP.

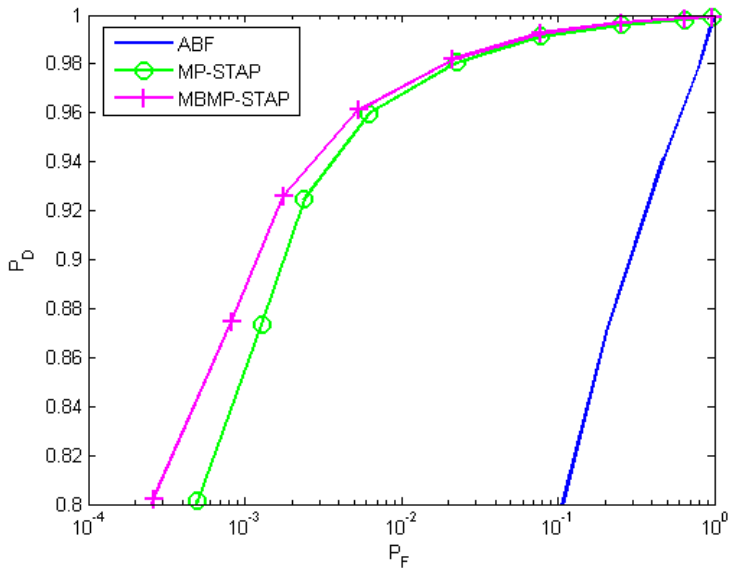

Figure 3.4 ROC curve for the ABF and MP-STAP with a $Z = 8\lambda$ MIMO random array with $N_t = 2$ and $N_r = 4$. There are two targets, one target has the angle-Doppler pair $(u = 0, f = 1/N_p)$ the other target has the angle-Doppler pair $(u = 0, f = -1/N_p)$. Parameters used: $K = 2$, SNR=18dB, CNR = 30dB

3.5 Concluding Remarks

In this chapter three detection algorithms the ABF, MP-STAP, and the MBMP-STAP were considered. The ABF, a popular method for GMTI radar divides the angle-Doppler map into G resolution cells and performs G detection tests, one for each resolution cell for the presence of a target. The number of targets is obtained by counting the number of cells that pass the detection test, and the positions of the targets depend on the cells that pass the test. The detection test that was considered for the beamformer was the AMF. While simple to implement, the beamformer suffers from the high sidelobes of the MIMO random array causing the algorithm to experience a high false alarm rate.

On the other hand, MP-STAP relies on the sparsity of the targets which allows one to cope with the high sidelobes of the MIMO random array while taking advantage of the high resolution of the MIMO random array. The MP-STAP localizes $\overline{K}$ candidate target locations by using a MP algorithm where $\overline{K}$ is the upper bound

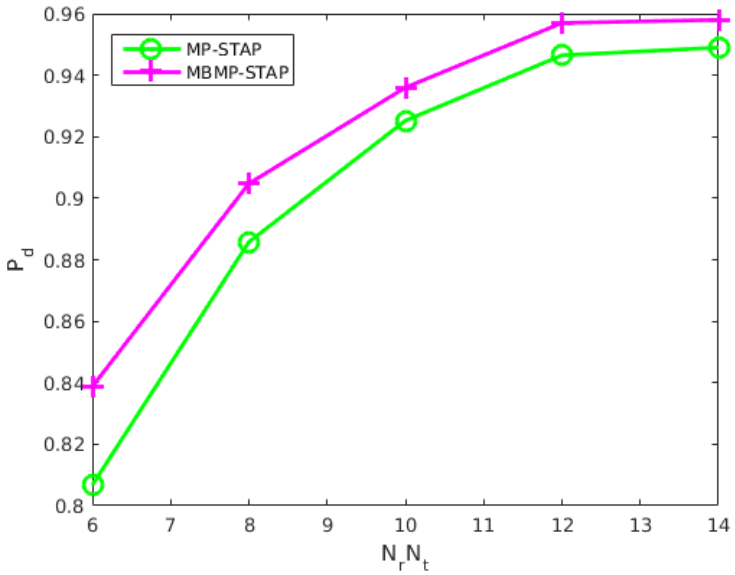

Figure 3.5 Probability of detection vs $N_t N_r$ for MP-STAP and MBMP-STAP with a $Z = 8\lambda$ MIMO random array. There are two targets, one target has the angle-Doppler pair $(u = 0, f = 1/N_p)$ the other target has the angle-Doppler pair $(u = 0, f = -1/N_p)$. Parameters used: $K = 2$, SNR=18dB, CNR = 30dB

on the number of targets. The $\overline{K}$ target locations are then tested for the presence of a target, if one or more target locations fails the detection test, $\overline{K}$ is decreased by one and the algorithm is reran with the new value of $\overline{K}$. If all the target locations obtained by MP passes a detection test, the algorithm terminates and outputs all $\overline{K}$ target locations as the solution.

The MBMP-STAP generalizes the MP-STAP algorithm and considers multiple candidates for the first target as opposed to just one candidate as in MP-STAP. MBMP-STAP also considers multiple candidates for the second and subsequent targets. This generalization decreases the probability of false alarm caused by localizing a target in the wrong resolution cell. This generalization was demonstrated to improve the performance of the radar when multiple targets exist on the angle-Doppler map. Numerical examples demonstrate that both MP-STAP and MBMP-STAP significantly outperform the ABF when a MIMO random array is employed. In particular, numerical results indicate that MBMP-STAP can achieve

the same detection performance as the ABF but experiences roughly $10^{-}2$ times less false alarms than the ABF.

CHAPTER 4

CFAR SPARSITY BASED GMTI RADAR

In the previous chapter, a sparsity based radar based on [55] was presented. More specifically, the detection algorithm presented in [55] was modified for airborne radar using STAP. Numerical examples showed that sparsity based radar outperform the ABF when a MIMO random array is utilized. However, there are two drawbacks to both the MP-STAP and the MBMP-STAP algorithms. First, both sparsity based algorithms require some knowledge of the number of targets. More specifically, both algorithms require an upper bound on the number of targets, in radar applications this information may be unavailable. Another drawback is the detector specified in [55] was designed for an interference background of white Gaussian noise. When this assumption holds, the statistics of the detector are well specified. In STAP however, the interference covariance matrix is colored and unknown. This causes difficulties in analyzing the statistics of the detector making a CFAR detector difficult to obtain.

In this chapter, new detection algorithms for airborne radar are proposed which combine the strengths of MIMO random arrays with the ability of sparsity based algorithms to handle undersampling effects. Two sparsity-based CFAR detection algorithms are proposed in this chapter, referred to as matching pursuit-CFAR (MP-CFAR) and multibranch MP-CFAR (MBMP-CFAR), respectively. MP-CFAR consists of a target localization stage followed by a target detection stage. MBMP-CFAR generalizes MP-CFAR by maintaining and updating multiple sets of candidate targets. The new detectors do not require *any* knowledge on the number of targets and the statistics of the new detectors are derived in this chapter. As its name suggests, both MP-CFAR and MBMP-CFAR are CFAR detectors, in the sense that the statistics of the new detectors do not depend on the interference covariance matrix.

4.1 Detection by Adaptive Beamforming

In this section, the statistics of the ABF is reviewed, it will later be used as a benchmark for the proposed detectors. Recall that the test statistic of the ABF for a resolution cell specified by the steering vector $\mathbf{a}$ is given by

$$T = \frac{|\mathbf{a}^H \widehat{\mathbf{R}}^{-1}\mathbf{y}|^2}{\mathbf{a}^H \widehat{\mathbf{R}}^{-1}\mathbf{a}} \geq \gamma. \tag{4.1}$$

An alternative form of the test statistic that will be useful later for performance evaluation can be found applying an approach from [72] and [73]. In particular, it is shown in [73] that the test for deciding H_1 (4.1) may be expressed as the ratio of two independent random variables

$$T = \frac{|\zeta|^2}{\psi} \geq h\gamma. \tag{4.2}$$

Where ζ is distributed $CN(0,1)$ when a target is not present and $CN\left(\sqrt{h\rho},1\right)$ when a target with steering vector $\mathbf{a}_t$ is present, where the target's SINR is given by

$$\rho = \frac{\left|x\mathbf{a}^H \mathbf{R}^{-1}\mathbf{a}_t\right|^2}{\mathbf{a}^H \mathbf{R}^{-1}\mathbf{a}}. \tag{4.3}$$

The test statistic (4.2) tests for the presence of a target by applying a steering vector $\mathbf{a}$, but the actual steering vector of the target is $\mathbf{a}_t$. The denominator of (4.2), ψ, is a chi-squared random variable with $2(L+1-N)$ degrees of freedom. Since the factor $(L+1-N)$ appears in several expressions in the sequel, for notational brevity, let $M \triangleq (L+1-N)$. The factor h, first proposed in [74] is a loss factor $0 \leq h \leq 1$ that captures the effect of estimating the covariance matrix from the secondary data. It is shown in [75] that in the absence of a target, the probability density function (PDF) of the loss factor is the beta PDF

$$p(h) = p_\beta(h; M+1, N-1) = \frac{(N+N-1)!}{M!(N-2)!} h^M (1-h)^{N-2}. \tag{4.4}$$

When a target is present, it was shown in [76] the PDF of the loss factor is given by

$$\begin{aligned} p(h) =& e^{-Ch} \sum_{m=0}^{M+1} \binom{M+1}{m} \frac{(N+M-1)!}{(N+M-1+m)!} \\ & \times C^m p_\beta(h; M+1, N-1+m). \end{aligned} \tag{4.5}$$

Where the term C is defined as

$$C = |x|^2 \mathbf{a}_t^H \mathbf{R}^{-1} \mathbf{a}_t \left(1 - \frac{|\mathbf{a}^H \mathbf{R}^{-1} \mathbf{a}_t|^2}{(\mathbf{a}^H \mathbf{R}^{-1} \mathbf{a})(\mathbf{a}_t^H \mathbf{R}^{-1} \mathbf{a}_t)} \right). \tag{4.6}$$

The numerator $|\zeta|^2$ of the test statistic (4.2) is the squared magnitude of a complex-valued Gaussian random variable with zero mean or non-zero mean, depending on whether a target is present or not. It follows that $|\zeta|^2$ is a central or non-central chi-squared random variable with 2 degrees of freedom. The test statistic T is then the ratio of two independent chi-square random variables. Normalizing the numerator and the denominator by the respective degrees of freedom and adjusting the threshold accordingly yields the test

$$T = \frac{|\zeta|^2/2}{\psi/2M} \geq hM\gamma. \tag{4.7}$$

Conditioned on the loss factor h, when there is no target present, the test statistic follows the central F distribution with parameters 2 and $2M$, denoted $F(2, 2M)$. When there is a target present, the test statistic follows the non-central F distribution with parameters 2 and $2M$, and non-centrality parameter $h\rho$, denoted $F(2, 2M, h\rho)$.

From the previous discussion, the probability of false alarm conditioned on the loss factor h, is given by

$$\Pr\{T \geq h\gamma | h\} = 1 - \Phi_{F(2,2M)}(hM\gamma | h), \tag{4.8}$$

where $\Phi_{F(\cdot,\cdot)}$ denotes the CDF of the F distribution $F(\cdot,\cdot)$. The unconditioned probability of false alarm is obtained by averaging $\Pr\{T \geq h\gamma|h\}$ over h

$$P_{FA} = 1 - \int_0^1 \Phi_{F(2,2M)}(hM\gamma|h)p(h)dh \tag{4.9}$$

where $p(h)$ is given by (4.4). Note that the system has a CFAR property in the sense that the probability of false alarm is a function of the number of degrees of freedom M and N, but is not dependent on the clutter or noise (it is not a function of the interference and noise covariance matrix $\mathbf{R}$)

The conditional probability of detection of a target with SINR ρ (4.3) is given by

$$\Pr\{T \geq h\gamma|h\} = 1 - \Phi_{F(2,2M,h\rho)}(hM\gamma|h), \tag{4.10}$$

The unconditional probability of detection is

$$P_D = 1 - \int_0^1 \Phi_{F(2,2M,h\rho)}(hM\gamma|h)p(h)dh \tag{4.11}$$

where $p(h)$ is given by (4.5). These expressions will be used in the numerical results section to evaluate performance and compare it with the proposed sparsity based CFAR radar.

As previously discussed , a typical application of STAP is to perform test (4.2) for each of the resolution cells of interest. A STAP system designed as described in this section is CFAR because its false alarms are independent of the clutter and noise. Moreover, the CFAR property relies on the assumption that targets do not cause false alarms due to energy leaked through the sidelobes. This is equivalent to assuming that the numerator term in (4.3), $\mathbf{a}^H\mathbf{R}^{-1}\mathbf{a}_t$ is negligible when $\mathbf{a} \neq \mathbf{a}_t$. For ULAs, this assumption is valid since the peak sidelobe of a ULA (the steering vector $\mathbf{a}$ with $\mathbf{a} \neq \mathbf{a}_t$ that maximizes (4.3)) is roughly –13 dB relative to the mainlobe (when $\mathbf{a} = \mathbf{a}_t$). However, this assumption breaks down in a MIMO random array in which

the beampattern sidelobes cannot be assumed to be negligible. Such a system is not CFAR anymore. In the next section, an approach that preserves the CFAR property even for MIMO random arrays is proposed.

4.2 MP-CFAR Radar

In the previous section, it was noted that a traditional detection approach in which resolution cells are tested for target presence ignoring possible interference from other resolution cells, may fail when applied to MIMO random arrays STAP. In this section, an approach that relies on the sparsity of targets. It is also shown that it is well suited to handle data collected by MIMO random arrays.

Recall from Chapter 3 that MP-STAP approximates the solution to the optimization problem

$$\min_{\mathbf{x}} \|\mathbf{z} - \mathbf{B}\mathbf{x}\|_2^2 \text{ subject to } \|\mathbf{x}\|_0 \leq K. \tag{4.12}$$

Recall that to solve (4.12) one requires the knowledge of number of targets K, which of course is unknown apriori. To circumvent this issue in the previous chapter, $\overline{K}$, the upper bound on the number of target was used in conjunction with a detector. This procedure creates a produces a sparsity based radar that unfortunately, requires an upper bound on the number of targets. In addition the statistics for the radar is unavailable making the design of a CFAR sparsity based radar difficult.

To implement a CFAR radar that exploits target sparsity, a two-stage detection algorithm is proposed and is referred to as the MP-CFAR detection algorithm. Candidate targets are localized in the first phase; in the second phase, the candidate targets are tested for detection. A detected target is canceled from the data. The cancellation of detected targets from the data is intended to remove mutual interference between targets and thus address one of the flaws of detection by ABF,

as discussed in the previous section. A block diagram of the MP-CFAR algorithm is shown in Figure 4.1.

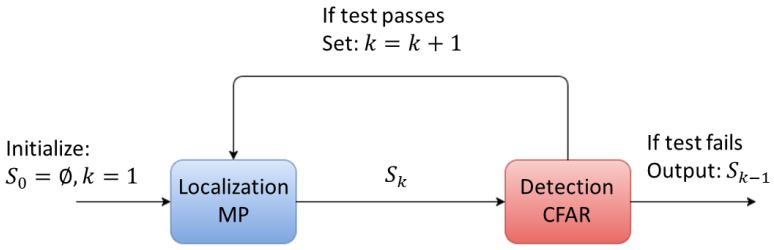

Figure 4.1 Block diagram of the MP-CFAR algorithm.

Note that in MP-STAP one localizes $\overline{K}$ targets then performs detection. It then updates the upper bound $\overline{K}$ if the detector finds that one or more of the $\overline{K}$ targets do not pass the detection test. In MP-CFAR, once a target is localized it is immediately tested by a detector. The algorithm terminates whenever a localized target does not pass a detection test therefore bypassing the need for $\overline{K}$.

4.2.1 Stage 1: MP Localization

The first pass of the MP localization algorithm uses whitened data $\mathbf{z} = \widehat{\mathbf{R}}^{-1/2}\mathbf{y}$ and whitened steering vectors $\mathbf{b}_j = \widehat{\mathbf{R}}^{-1/2}\mathbf{a}_j$, $j = 1, ..., G$. The first candidate target is localized by the index m_1 of the vector $\mathbf{b}_j$ that has the largest data projection,

$$m_1 = \arg\max_j \frac{|\mathbf{b}_j^H \mathbf{z}|^2}{\mathbf{b}_j^H \mathbf{b}_j} \tag{4.13}$$

for $j = 1, ..., G$. The index m_1 localizes the target in the angle-Doppler domains. This information is subsequently used by the detection stage, as described in relation with Stage 2 below. Unlike in MP-STAP however, the detection stage occurs immediately after the localization of a target.

The localization of the k-th candidate target is described, given that $k-1$ targets have already been localized and passed the detection test. The steering vectors are

processed to cancel the contributions of previously detected targets. Let a matrix $\mathbf{B}$ be formed with the columns $\mathbf{b}_j$. Let S_{k-1} be the set of indices of columns of $\mathbf{B}$ associated with detected targets, and let $\mathbf{B}_{S_{k-1}}$ be the matrix formed by the columns indexed by S_{k-1}. The projection matrix orthogonal to the detected targets is given by $\mathbf{P}^{\perp}_{\mathbf{B}_{S_{k-1}}} = \mathbf{I} - \mathbf{B}_{S_{k-1}} \left(\mathbf{B}^H_{S_{k-1}} \mathbf{B}_{S_{k-1}} \right)^{-1} \mathbf{B}_{S_{k-1}}$. The steering vectors orthogonal to the detected targets are formed as follows: $\mathbf{w}_j = \mathbf{P}^{\perp}_{\mathbf{B}_{S_{k-1}}} \mathbf{b}_j$, for all $j \notin S_{k-1}$. The k-th target is localized according to

$$m_k = \arg\max_j \ \frac{|\mathbf{w}_j^H \mathbf{z}|^2}{\mathbf{w}_j^H \mathbf{w}_j} \tag{4.14}$$

This process continues until a candidate target fails the detection test.

4.2.2 Stage 2: Detection

The derivation of the CFAR detector that is applied to candidate targets localized in Stage 1 is now derived. The first candidate target is detected according to (4.1), rewritten here for convenience

$$T = \frac{|\mathbf{a}_{m_1}^H \widehat{\mathbf{R}}^{-1} \mathbf{y}|^2}{\mathbf{a}_{m_1}^H \widehat{\mathbf{R}}^{-1} \mathbf{a}_{m_1}} \geq \gamma, \tag{4.15}$$

where m_1 is the index found in Stage 1. Note that the test (4.15) may also be expressed in terms of the whitened steering vectors $\mathbf{b}_{m_1} = \widehat{\mathbf{R}}^{-1/2} \mathbf{a}_{m_1}$,

$$T = \frac{|\mathbf{b}_{m_1}^H \mathbf{z}|^2}{\mathbf{b}_{m_1}^H \mathbf{b}_{m_1}} \geq \gamma. \tag{4.16}$$

Next the detection of candidate target k, given that $k-1$ targets have been already localized and passed the detection test is described. The signal model is given by the expression

$$\begin{aligned} \mathbf{z} &= \mathbf{b}_{m_k} x_{m_k} + \mathbf{B}_{S_{k-1}} \mathbf{x}_{S_{k-1}} + \mathbf{n} \\ &= \mathbf{B}_{S_k} \mathbf{x}_{S_k} + \mathbf{n} \end{aligned} \tag{4.17}$$

where m_k is the index of the resolution cell of the k-th candidate target found in Stage1 (4.14), S_k is formed by adding m_k to the set S_{k-1}, $S_k = S_{k-1} \bigcup m_k$, the matrix $\mathbf{B}_{S_k} = \left[\mathbf{b}_{m_k}, \mathbf{B}_{S_{k-1}}\right]$ is the matrix formed by columns with indices in S_k, $\mathbf{x}_{S_k} = \left[x_{m_k}, \mathbf{x}_{S_{k-1}}^T\right]^T$, and $\mathbf{n} = \widehat{\mathbf{R}}^{-1/2}\mathbf{e}$. This signal model leads to the following detection test:

$$H_0 : x_{m_k} = 0$$

$$H_1 : x_{m_k} \neq 0$$

Here, the following problem is posed: detect a target located at a specified whitened steering vector $\mathbf{b}_{m_k}$ and having unknown amplitude, observed in the presence of interference and noise. The interference is of unknown gain $\mathbf{x}_{S_{k-1}}$, but belonging to a known subspace $\mathbf{B}_{S_{k-1}}$. The noise is Gaussian colored noise for which the covariance matrix is unknown, but secondary data is available for its estimation.

As in the discussion leading to (4.1), the covariance matrix is replaced with the sample covariance matrix $\widehat{\mathbf{R}}$ of the secondary data, thus $\mathbf{z} = \widehat{\mathbf{R}}^{-1/2}\mathbf{y}$ is modeled as having a covariance matrix equal to the identity matrix. It follows that under H_0, the likelihood is

$$p\left(\mathbf{z}|\mathbf{H}_0\right) = \frac{1}{\pi^N} e^{-\left(\mathbf{z}-\mathbf{B}_{S_{k-1}}\mathbf{x}_{S_{k-1}}\right)^H\left(\mathbf{z}-\mathbf{B}_{S_{k-1}}\mathbf{x}_{S_{k-1}}\right)},$$

while under H_1 the likelihood is

$$p\left(\mathbf{z}|\mathbf{H}_1\right) = \frac{1}{\pi^N} e^{-\left(\mathbf{z}-\mathbf{B}_{S_k}\mathbf{x}_{S_k}\right)^H\left(\mathbf{z}-\mathbf{B}_{S_k}\mathbf{x}_{S_k}\right)}.$$

The GLRT for deciding H_1 is given by

$$T = \ln\left(\frac{\max_{\mathbf{x}_{S_k}} p(\mathbf{z}|\mathbf{x}_{S_k})}{\max_{\mathbf{x}_{S_{k-1}}} p(\mathbf{z}|\mathbf{x}_{S_{k-1}})}\right) \geq \gamma \tag{4.18}$$

To obtain a more convenient form of the test, note that under hypothesis H_0, the MLE of the gain vector $\mathbf{x}_{S_{k-1}}$ is found from

$$\widehat{\mathbf{x}}_{S_{k-1}} = \min_{\mathbf{x}_{S_{k-1}}} \|\mathbf{z} - \mathbf{B}_{S_{k-1}}\mathbf{x}_{S_{k-1}}\|_2^2. \tag{4.19}$$

Minimizing (4.19) with respect to the vector of complex gains $\mathbf{x}_{S_k}$ yields

$$\widehat{\mathbf{x}}_{S_{k-1}} = (\mathbf{B}_{S_{k-1}}^H \mathbf{B}_{S_{k-1}})^{-1}\mathbf{B}_{S_{k-1}}^H \mathbf{z}. \tag{4.20}$$

Similarly,

$$\widehat{\mathbf{x}}_{S_k} = (\mathbf{B}_{S_k}^H \mathbf{B}_{S_k})^{-1}\mathbf{B}_{S_k}^H \mathbf{z}. \tag{4.21}$$

Inserting (4.20) and (4.21) into (4.18),

$$\begin{aligned} T &= \|\mathbf{z} - \mathbf{B}_{S_{k-1}}\widehat{\mathbf{x}}_{S_{k-1}}\|_2^2 - \|\mathbf{z} - \mathbf{B}_{S_k}\widehat{\mathbf{x}}_{S_k}\|_2^2 \\ &= \mathbf{z}^H \left(\mathbf{P}_{\mathbf{B}_{S_k}} - \mathbf{P}_{\mathbf{B}_{S_{k-1}}}\right)\mathbf{z} \end{aligned} \tag{4.22}$$

where $\mathbf{P}_{\mathbf{B}} = \mathbf{B}\left(\mathbf{B}^H\mathbf{B}\right)^{-1}\mathbf{B}$ is a projection matrix that projects onto the subspace spanned by $\mathbf{B}$. Note that the decision statistic is a difference between two quadratic forms, where the quadratic form $\mathbf{z}^H\mathbf{P}_{\mathbf{B}_{S_{k-1}}}\mathbf{z}$ is an interference term that is canceled.

The test statistic (4.22) may be further simplified, which will be useful to obtain expressions for performance evaluation of the MP-CFAR detector. To do so, the following result from [77] and [78] is used. Let $\mathbf{D}$ and $\mathbf{E}$ be two subspaces, and let $\mathbf{P}_{\mathbf{D}}$ and $\mathbf{P}_{[\mathbf{D},\mathbf{E}]}$ be projection matrices that project onto the subspaces spanned by the matrices $\mathbf{D}$ and $[\mathbf{D},\mathbf{E}]$, respectively. Let $\mathbf{F} = \mathbf{P}_{\mathbf{D}}^{\perp}\mathbf{E}$, then the difference between projection matrices $\mathbf{P}_{[\mathbf{D},\mathbf{E}]} - \mathbf{P}_{\mathbf{D}}$ is given by [78]

$$\mathbf{P}_{[\mathbf{D},\mathbf{E}]} - \mathbf{P}_{\mathbf{D}} = \mathbf{P}_{\mathbf{F}}. \tag{4.23}$$

Now, identify $\mathbf{D} = \mathbf{B}_{S_{k-1}}$ and $\mathbf{E} = \mathbf{b}_{m_k}$ (whitened steering vector). Then $\mathbf{F} = \mathbf{P}_{\mathbf{D}}^{\perp}\mathbf{E} = \mathbf{P}_{\mathbf{B}_{S_{k-1}}}^{\perp}\mathbf{b}_{m_k}$ is a vector, and let $\mathbf{f}_k \triangleq \mathbf{P}_{\mathbf{B}_{S_{k-1}}}^{\perp}\mathbf{b}_{m_k}$. Note that $\mathbf{f}_1 = \mathbf{b}_{m_1}$. Since by design, $\mathbf{f}_{k-1}$ is already orthogonal to all previous vectors $\mathbf{f}_1, ..., \mathbf{f}_{k-2,}$ one obtains the following recurrent relations

$$\mathbf{f}_k = \mathbf{P}_{\mathbf{f}_{k-1}}^{\perp}\mathbf{b}_{m_k}. \tag{4.24}$$

From this expression, $\mathbf{f}_k$ is the projection on the whitened steering vector $\mathbf{b}_{m_k}$ orthogonal to the previous $k-1$ targets. Applying (4.23), yields

$$\mathbf{P}_{\left[\mathbf{B}_{S_{k-1}}, \mathbf{b}_{m_k}\right]} - \mathbf{P}_{\mathbf{B}_{S_{k-1}}} = \mathbf{P}_{\mathbf{f}_k} \tag{4.25}$$

where $\mathbf{P}_{\mathbf{f}_k} = \mathbf{f}_k\mathbf{f}_k^H/\mathbf{f}_k^H\mathbf{f}_k$. Noting that $\mathbf{B}_{S_k} = \left[\mathbf{B}_{S_{k-1}}, \mathbf{b}_{m_k}\right]$ and substituting (4.25) into (4.22), the test for deciding H_1 on the detection of the k-th target can be expressed

$$T = \frac{|\mathbf{f}_k^H\mathbf{z}|^2}{\mathbf{f}_k^H\mathbf{f}_k} \geq \gamma \tag{4.26}$$

For $k = 1$, $\mathbf{f}_1 = \mathbf{b}_{m_1}$, and (4.26) reverts to (4.16) as it should.

The test statistic (4.26) is applied to every candidate target included in the set S_k. If any of the k tests fails to exceed the threshold γ, the algorithm terminates and outputs the set S_{k-1}, the set of $k-1$ target locations. Otherwise, MP CFAR increments the number of targets k by one and reruns MP with the new value of k. The psuedocode for the MP CFAR algorithm is listed in Algorithm 2.

4.2.3 Performance of the MP-CFAR Detector

In this part, the analytical expressions for the probability of false alarm and probability of detection of the MP-CFAR detector for some simple cases are developed. To obtain an expression for the probability of false alarm when no target is present in the field of view, the test statistic (4.26) is manipulated to express it in the form (4.7). By assumption, no target has been detected yet, hence the test is for

Algorithm 2 MP-CFAR

1: **Input**: $\mathbf{y}, \mathbf{A}, \hat{\mathbf{R}}, \gamma$.

2: **Initialize**: $S_0 = \emptyset$, $\mathbf{r} = \hat{\mathbf{R}}^{-1/2}\mathbf{y}$, $\mathbf{B} = \hat{\mathbf{R}}^{-1/2}\mathbf{A}$, $\mathbf{W} = \mathbf{B}$, $k = 1$.

3: **Find**: Search for the index l that maximizes the metric $\max_j \ |\mathbf{w}_j^H \mathbf{r}|^2 / \mathbf{w}_j^H \mathbf{w}_j$.

4: **Update set of targets**: $S_k = S_{k-1} \bigcup l$.

5: **Check**: **If** $T_{s_i} \geq \gamma$ (test statistic to decide if x_{s_i} is nonzero) for all $s_i \in S_k$ continue. **Otherwise** output S_{k-1} as solution and terminate.

6: **Generate**: $\mathbf{P}^{\perp}_{\mathbf{B}_{S_k}} = \mathbf{I} - \mathbf{B}_{S_k} \left(\mathbf{B}_{S_k}^H \mathbf{B}_{S_k} \right)^{-1} \mathbf{B}_{S_k}^H$.

7: **Remove found targets**: $\mathbf{W} = \mathbf{P}^{\perp}_{\mathbf{B}_{S_k}} \mathbf{B}$.

8: **Renormalize**: **If** $\|\mathbf{w}_i\|_2 = 0$, set $\mathbf{w}_i = \mathbf{0}$.

9: **Return to step 3**

target index $k = 1$. For $k = 1$, and based on notation developed previously, the vector $\mathbf{f}_{s_1} = \mathbf{b}_{m_1} = \widehat{\mathbf{R}}^{-1/2}\mathbf{a}_{m_1}$ and $\mathbf{z} = \widehat{\mathbf{R}}^{-1/2}\mathbf{y}$. Now recall that m_1 is the index obtained from (4.14). It follows that (4.26) may be written

$$T = \max_j \frac{|\mathbf{a}_j^H \widehat{\mathbf{R}}^{-1} \mathbf{y}|^2}{\mathbf{a}_j^H \widehat{\mathbf{R}}^{-1} \mathbf{a}_j} \tag{4.27}$$

Other than the max operator, the test statistic in (4.27) is of the form (4.1), hence it can be reduced to the form (4.7),

$$T = \max_j \ \Gamma_j, \tag{4.28}$$

where

$$\Gamma_j = \frac{|\zeta_j|^2/2}{\psi_j/2M}. \tag{4.29}$$

The probability of false alarm is given by

$$P_{FA} = 1 - \Pr\left\{ \max_j \Gamma_j \leq hM\gamma \right\}$$

Since the random variables Γ_j (4.29) are independent and identically distributed,

$$P_{FA} = 1 - \left(\Pr\left\{\Gamma_j \leq hM\gamma\right\}\right)^G$$

As discussed in relation with (4.8), Γ_j follows an F distribution with CDF $\Phi_{F(2,2M)}$, from which the expression for the probability false alarm

$$P_{FA} = 1 - \left(\int_0^1 \Phi_{F(2,2M)}(hM\gamma|h)p(h)dh\right)^G \tag{4.30}$$

The probability of detection of the first target is given by the same expression as for the ABF, (4.11).

4.3 MBMP CFAR

The MP-CFAR algorithm localizes the first target according to (4.13), namely, finds the column of the whitened measurement matrix with the largest projection on the whitened data $\mathbf{z}$. A false alarm (localizing the target in the wrong resolution cell) increases the chance of further false alarms downstream, since according to (4.14), localizing subsequent candidate targets depends on the location of the first target (4.13). As with MBMP-STAP, a more robust approach is to hedge bets by finding multiple candidates for the location of the first target. Each such candidate target serves as seed to the localization and detection of subsequent targets. When the process is completed, a metric is used to select the set of targets that provides the best fit to the data. This algorithm, which generalizes MP-CFAR is referred to as MBMP-CFAR.

Recall from the previous chapter, a localization solution is referred to as a branch. The set $D = \{d_1, d_2, ..., d_k\}$ contains the number of branches per target. A path is a sequence of branches specified by their index numbers. For example the path $(i_1, i_2, ..., i_k)$, $1 \leq i_1 \leq d_1, ..., 1 \leq i_k \leq d_k$. A localization solution $1 \leq m_k^{(i_1,i_2,...,i_k)} \leq G$, where G is the number of resolution cells (see (2.7)), consists of a path and the

index number of the resolution cell. The set $S_k^{(i_1,...,i_k)} = \left\{m_1^{(i_1)}, m_2^{(i_1,i_2)}, ..., m_k^{(i_1,...,i_k)}\right\}$ contains the localization solution associated with path $(i_1, i_2, ..., i_k)$. For k candidate targets, MBMP-CFAR maintains $d_1 \times d_2 \times ... \times d_k$ such sets. The matrix $\mathbf{B}_{S_k}$ was defined to consist of the whitened steering vectors $\mathbf{b}_j$ indexed by S_k.

4.3.1 Stage 1: MBMP Localization

The inputs to MBMP-CFAR are the whitened measurement vector $\mathbf{z} = \widehat{\mathbf{R}}^{-1/2}\mathbf{y}$, whitened steering vectors $\mathbf{b}_j = \widehat{\mathbf{R}}^{-1/2}\mathbf{a}_j$, $j = 1, ..., G$, and a set of positive integers $D = \{d_1, d_2, \ldots, d_G\}$. Similar to MP-CFAR, the MBMP-CFAR algorithm proceeds in two stages. To localize the candidates for the first target, the algorithm finds the d_1 indices $m_1^{(1)}, m_1^{(2)}, \ldots, m_1^{(d_1)}$ that produce the d_1 largest projections of steering vectors $\mathbf{b}_j$ on the data $\mathbf{z}$. Specifically, the resolution cell index that localizes the first branch of the first target is found from

$$m_1^{(1)} = \arg\max_j \frac{|\mathbf{b}_j^H \mathbf{z}|^2}{\mathbf{b}_j^H \mathbf{b}_j} \tag{4.31}$$

The i-th branch of the first target, $1 \leq i \leq d_1$, is found from

$$m_1^{(i)} = \arg \max_{j \notin \{m_1, ..., m_{i-1}\}} \frac{|\mathbf{b}_j^H \mathbf{z}|^2}{\mathbf{b}_j^H \mathbf{b}_j}. \tag{4.32}$$

Once all d_1 indicies are obtained MBMP-CFAR tests the resolution cell $m_1^{(i)}$ is tested for the presence of a target. If the target at $m_1^{(i)}$ passes the detection test, MBMP-CFAR continues to localize the second target. To generate the d_2 branches associated with the second target, define the modified steering vectors $\mathbf{w}_j^{(i)} = \mathbf{P}^{\perp}_{\mathbf{b}_{m_1^{(i)}}} \mathbf{b}_j$, for $1 \leq i \leq d_1$. The orthogonal projection prevents interference from a target at $m_1^{(i)}$. The resolution cell index associated with the first branch of the second target is given

by

$$m_2^{(1,1)} = \arg\max_j \frac{|\mathbf{w}_j^{(1)H}\mathbf{z}|^2}{\mathbf{w}_j^{(1)H}\mathbf{w}_j^{(1)}} \tag{4.33}$$

whereas the index of branch i_2, $1 \leq i_2 \leq d_2$ of the second target, given the path (i_1, i_2),

$$m_2^{(i_1,i_2)} = \arg\max_{j \notin \left\{m_1,\ldots,m_{i_2-1}\right\}} \frac{|\mathbf{w}_j^{(i_1)H}\mathbf{z}|^2}{\mathbf{w}_j^{(i_1)H}\mathbf{w}_j^{(i_1)}} \tag{4.34}$$

Generalizing to k targets and the path $(i_1, i_2, ..., i_k)$, define the vector $\mathbf{w}_j^{(i_1,\ldots,i_k)} = \mathbf{P}^{\perp}_{\mathbf{B}_{S_{k-1}^{(i_1,\ldots,i_{k-1})}}}\mathbf{b}_j$. The index associated with the k-th target is given by

$$m_k^{(i_1,\ldots,i_k)} = \arg\max_{j \notin \left\{m_1,\ldots,m_{i_k-1}\right\}} \frac{\left|\mathbf{w}_j^{(i_1,\ldots,i_{k-1})H}\mathbf{z}\right|^2}{\mathbf{w}_j^{(i_1,\ldots,i_{k-1})H}\mathbf{w}_j^{(i_1,\ldots,i_{k-1})}} \tag{4.35}$$

The process of MBMP localization continues until the detection test fails, as explained in relation with Stage 2.

4.3.2 Stage 2: Detection

The MBMP localization processing yielded d_1 candidate locations for the first target. The largest score relative to the objective function $|\mathbf{b}_j^H\mathbf{z}|^2/\mathbf{b}_j^H\mathbf{b}_j$ is obtained by the steering vector index $m_1^{(1)}$, because $\max_j |\mathbf{b}_j^H\mathbf{z}|^2/\mathbf{b}_j^H\mathbf{b}_j \geq \max_{j\notin\{m_1,\ldots,m_{i-1}\}} |\mathbf{b}_j^H\mathbf{z}|^2/\mathbf{b}_j^H\mathbf{b}_j$ (see (4.31) and (4.32)). Note that the choice of $m_1^{(1)}$ also minimizes the residual of the objective function $\|\mathbf{z} - \mathbf{B}\mathbf{x}\|_2^2$ (see (4.12)), $m_1^{(1)} = \arg\min_j \|\mathbf{P}^{\perp}_{\mathbf{b}_j}\mathbf{z}\|_2^2$. The test to determine whether a target is present in the resolution cell $m_1^{(1)}$ is given by (see (4.26))

$$T = \frac{|\mathbf{b}^H_{m_1^{(1)}}\mathbf{z}|^2}{\mathbf{b}^H_{m_1^{(1)}}\mathbf{b}_{m_1^{(1)}}} \geq \gamma \tag{4.36}$$

If the test (4.36) is met, d_1 target sets are updated as follows $S_1^{(i_1)} = \left\{m_1^{(i_1)}\right\}$, $1 \leq i_1 \leq d_1$.

To test for the detection of the k-th target, assume that $k-1$ targets have been detected. The residual along the path $(i_1, i_2, ..., i_k)$ is computed from

$$R^{(i_1,...,i_k)} = \left\| \mathbf{P}^{\perp}_{\mathbf{B}_{S_k^{(i_1,...,i_k)}}} \mathbf{z} \right\|_2^2$$

The path that yields the lowest residual is given by

$$(i_1, i_2, ..., i_k) = \arg \min_{(j_1,...,j_k)} R^{(j_1,...,j_k)}$$

The test to determine whether a target is present in the resolution cell $m_k^{(i_1,...,i_k)}$ is given by

$$T = \frac{|\mathbf{f}_k^{(i_1,...,i_k)} \mathbf{z}|^2}{\mathbf{f}_k^{(i_1,...,i_k)H} \mathbf{f}_k^{(i_1,...,i_k)}} \geq \gamma \tag{4.37}$$

If the test (4.37) is met, $d_1 \times ... \times d_k$ target sets are updated as follows $S_k^{(i_1,...,i_k)} = \left\{ m_1^{(i_1)}, m_2^{(i_1,i_2)}, ..., m_k^{(i_1,...,i_k)} \right\}$, $1 \leq i_1 \leq d_1, ..., 1 \leq i_k \leq d_k$. The MBMP-CFAR algorithm proceeds to the localization and detection of the $(k+1)$ target. If the detection test fails, MBMP-CFAR outputs as solution the path

$$(i_1, i_2, ..., i_{k-1}) = \arg \min_{(j_1,...,j_{k-1})} R^{(j_1,...,j_{k-1})}.$$

Similar to MBMP-STAP, the MBMP-CFAR algorithm generalizes the MP-CFAR by allowing the consideration of resolution cells that do not maximize the metric in (4.14). By allowing the algorithm the freedom to test more resolution cells the probability of false alarm due to localizing target in the incorrect resolution cell decreases.

4.4 Numerical Results

In this section, numerical results on the MP-CFAR and MBMP-CFAR algorithms are presented and compared to against the ABF. Unless stated otherwise, in figures presented in this section, the aperture of the MIMO random arrays is 8λ ($Z = 8$, where recall that Z is expressed in units of wavelength). The number of transmit elements in the random array is $N_t = 2$, and the number receive elements is given by $N_r = 4$. The number of coherent pulses used by all arrays is $N_p = 16$. The SNR, defined as $|x|^2/\sigma^2$ is set to SNR $= 100/N = -1.0721$ dB unless stated otherwise, where $N = N_t N_r N_p$, the clutter-to-noise ratio (CNR) is set to 30 dB. The number of training samples used to estimate the covariance matrix for the random array is $L = 2N$. The number of resolution cells on the angle-Doppler map is given by $G = (2Z + 1)^2 = 289$. For all figures, a random realization of a random array is generated and remains fixed throughout the Monte Carlo simulations. Let S_t be the true set of resolution cells that contain targets, and let $\hat{S}$ be the set of resolution cells found by a detector to have targets. A false alarm event occurs is $\hat{S} \setminus S_t \neq \emptyset$, and a detection event occurs if $\hat{S} \bigcap S_t \neq \emptyset$.

The probability of false alarm of the MP-CFAR detector is plotted vs. the detection threshold in Figure 4.2 for two scenarios. The first scenario is when no targets are present anywhere in the angle-Doppler map, the second scenario is when a single target is present at an arbitrary, fixed location with SNR = 20 dB. To obtain the curves the results of 10^4 Monte-Carlo simulations were averaged. The analytical probability of false alarm of the MP-CFAR obtained from (4.30) is also shown for reference. The figure illustrates that (4.30) accurately represent the probability of false alarm for the MP-CFAR detector and that the presence of targets in the field of view does not affect the probability of false alarm. In other words, MP-CFAR preserves its CFAR capability in spite of the higher sidelobes associated with the random array.

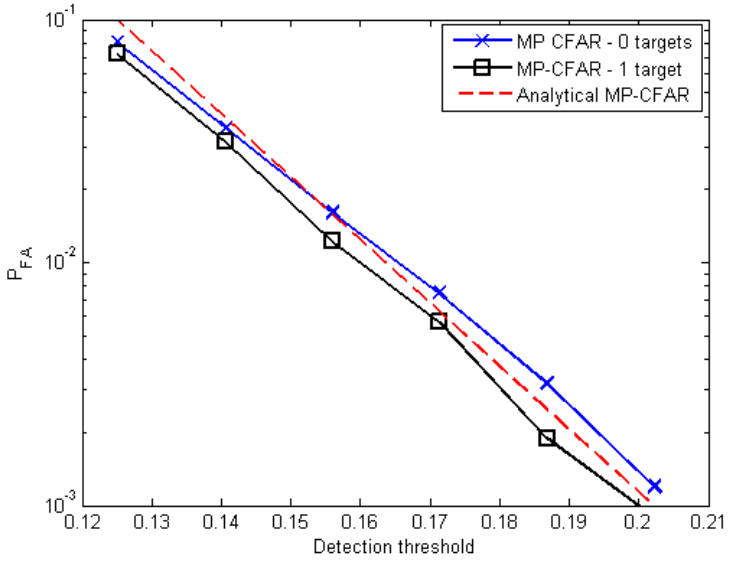

Figure 4.2 Probability of false alarm vs the detection threshold of the MP-CFAR detector. The number of next to the label in the legend corresponds to the number of targets that interfere with the detection test. The SNR of all targets is SNR=20dB.

The probabilities of false alarm of the MP-CFAR and ABF detectors are further studied in Figure 4.3, which plots the probability of false alarm against the SNR of a target present at an arbitrary resolution cell. The detection threshold for the ABF detector is set using (4.9), such that $P_{FA} = 10^{-3}$. Applying (4.30), the detection threshold for the MP-CFAR detector is also set to $P_{FA} = 10^{-3}$. Also plotted is the probability of false alarm of an ABF detector implemented by an 8λ ULA. For all scenarios, the results of 10^4 Monte-Carlo experiments were averaged to obtain the curves, the ABF tested every resolution cell on the angle-Doppler map. The probability of false alarm of a true CFAR detector should not change as a function of SNR of a target present somewhere in the search area. It is observed from the figure that the 8λ ULA ABF and the random array MP-CFAR detectors have probabilities of false alarm that are little changed as a function of the SNR of a target. More specifically, at low SNR the MP-CFAR experiences a probability of false alarm of about 2×10^{-3} instead of $P_{FA} = 10^{-3}$. This slight increase in the probability of false

alarm occurs because at low SNR, the probability of correct recovery (the probability that MP-CFAR recovers the correct resolution cell to test) is less than one. As the SNR of the target increases, the probability of correct recovery increases, and the false alarm probability of MP-CFAR decreases to $P_F = 10^{-3}$ as intended. It is noticed that the ABF using a 8λ ULA experiences a slight increase in the probability of false alarm as the SNR of the interfering target increases. This is because although the peak sidelobe of a ULA is small, it is not zero and therefore will ultimately affect the probability of false alarm. In contrast, a random array ABF cannot cope with energy leaked by high sidelobes, and as the strength of the target increases, the probability of false alarm increases.

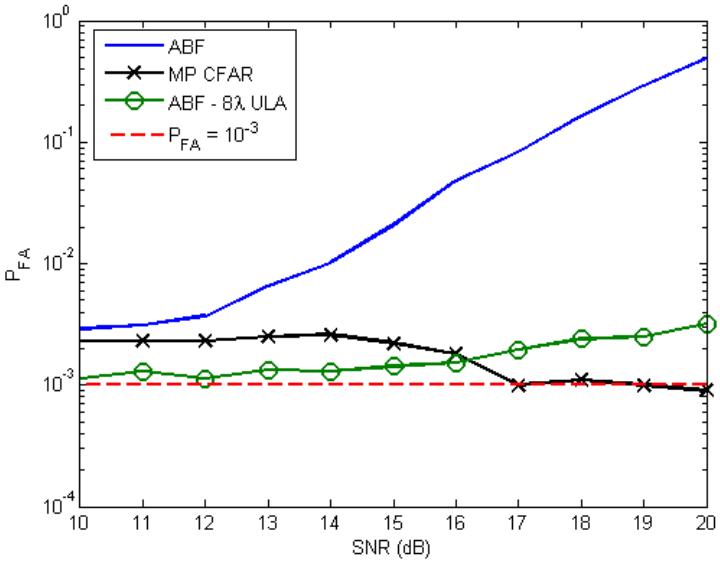

Figure 4.3 Probability of false alarm vs the SNR of a target in a different resolution cell for the ABF using a ULA with $Z = 4\lambda$ and $Z = 8\lambda$ and the detector of MP-CFAR using a random array. The number of next to the label (if present) in the legend corresponds to the number of targets that interfere with the detection test. The SNR of all targets is SNR = 20 dB.

In Figure 4.4, the probability of detection of the MP-CFAR detector is plotted against the SNR for one and two targets, respectively. The threshold parameter is set such that the probability of false alarm of the detector is $P_{FA} = 10^{-3}$. In

the first experiment, a single target is placed at an arbitrary fixed location in the angle-Doppler map. In the second experiment, to the first target is added a second target at a location that changes randomly between Monte Carlo runs. From the figure, it is seen that the probability of detection in the absence of an interfering target is slightly higher at higher SNRs. This slight decrease in performance when two targets are present in the field of view is attributed to the orthogonal projection performed when generating the steering vector in (4.24).

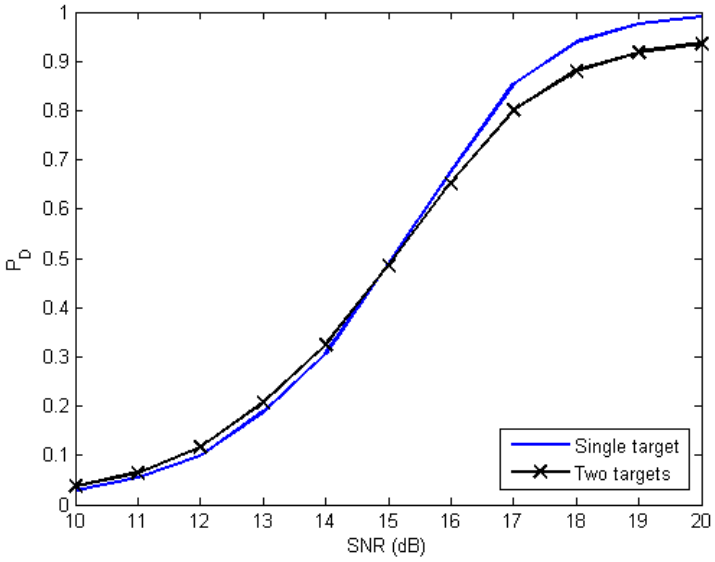

Figure 4.4 Probability of detection vs the SNR of a target in a different resolution cell for the MP-CFAR detector

In Figure 4.5 are shown the receiver operating curves (ROC) for a single target in the field of view and four cases: (1) 4λ ULA with ABF, (2) 8λ ULA with ABF,(3) 8λ random array (RA) with ABF, (4) 8λ RA with MP-CFAR. The target is placed at $(u = 0, f = 1/N_p)$, near the clutter ridge in the angle-Doppler map. To obtain a fair comparison, the normalization term in equation (2.5) is discarded so that the effect of the processing gain of each array is present. From the figure, it is observed that the 4λ ULA and 8λ RA using ABF perform significantly worse than the 8λ ULA using ABF. Since the 8λ ULA has sufficient resolution capability to resolve

target and clutter, it performs well as expected. The 4λ ULA cannot provide the angle-Doppler resolution required to resolve the target and clutter. Put it another way, the lower resolution array cannot discriminate between the target and the clutter ridge. The 8λ RA is hampered by the sidelobes of the random array, which lead to increased false alarms, and therefore has poor performance. In contrast, a significant performance gain is observed using the proposed random array MP-CFAR detector. The performance gain is attributed to the interference cancellation performed by the MP-CFAR detector compensating for the effect of the high sidelobes of the random array. Note that for $P_F \geq 10^{-3}$, the performance of the MP-CFAR detector is close to that of the 8λ ULA ABF detector despite the fact that the random array uses half the number of elements than that of the 8λ ULA. This demonstrates the savings without loss of performance that are gained by random arrays and the proposed MP-CFAR detector.

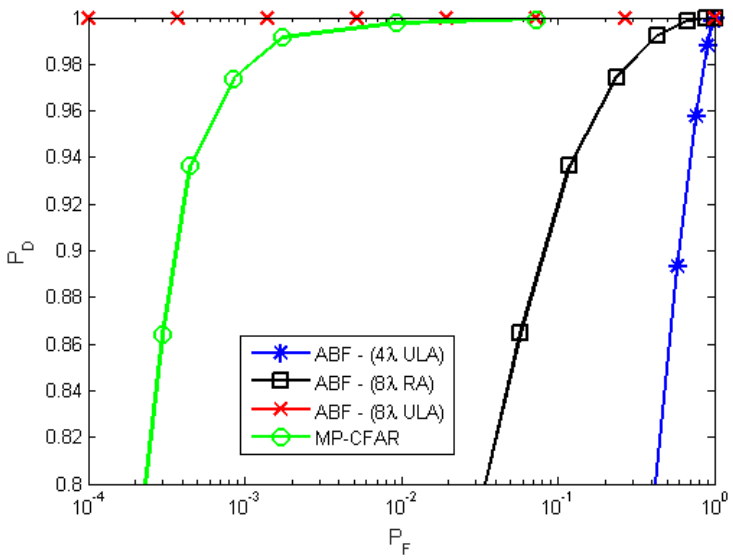

Figure 4.5 ROC curve for the ABF with a $Z = 4\lambda$ ULA, ABF with a $Z = 8\lambda$ random array, MP-CFAR with a $Z = 8\lambda$ random array and the ABF with a $Z = 8$ ULA for the random arrays the number of sensors used was $N = 8$. The target has the angle-Doppler pair $(u = 1/Z, f = 0)$. Parameters used: $K = 1$, SNR=20dB, CNR = 30dB

Figure 4.6 presents the ROC curve for two targets are present in the angle-Doppler map associated with a range cell. Five cases are shown: (1) 4λ ULA with ABF, (2) 8λ ULA with ABF, (3) 8λ random array (RA) with ABF, (4) 8λ RA with MP-CFAR, (5) 8λ RA with MBMP-CFAR. The normalization term in equation (2.5) is again discarded for a fair comparison. The number of branches for the MBMP-CFAR detector is given by $D = \{5,\ 1,\ 1,\ \ldots\}$. Two targets with spatial frequency $u = 0$ are placed on the angle-Doppler map. Both targets are slowly moving, one target has a Doppler $1/N_p$ while the other has a Doppler of $-1/N_p$. As in the single target case, the 8λ ULA with ABF performs well, while the 4λ ULA and the 8λ RA with ABF perform poorly. The MP-CFAR and MBMP-CFAR detectors significantly outperform the smaller ULA and the RA with ABF. The MBMP-CFAR also outperforms the MP-CFAR in terms of the false alarm probabilities.

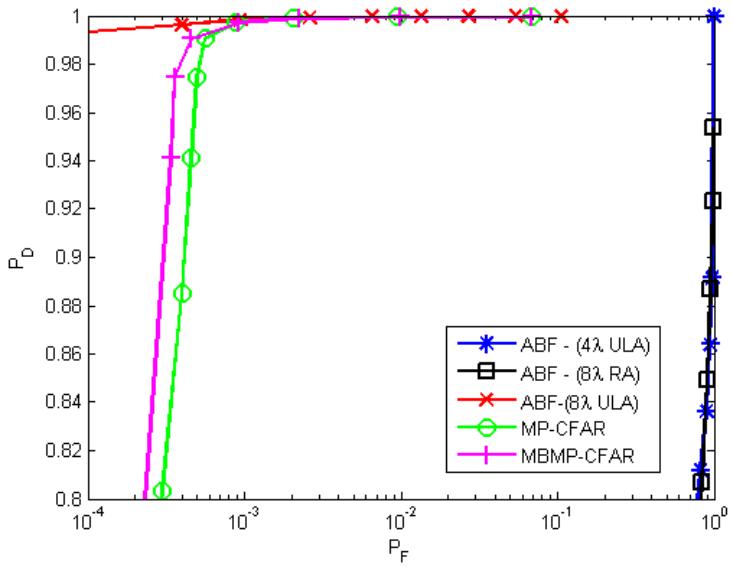

Figure 4.6 ROC curve for the ABF with a $Z = 4\lambda$ ULA, ABF with a $Z = 8\lambda$ random array, MP-CFAR with a $Z = 8\lambda$ random array, MP-CFAR with a $Z = 8\lambda$ random array, and the ABF with a $Z = 8$ ULA for the random arrays the number of sensors used was $N = 8$. Parameters used: $K = 1$, SNR = -1.0721 dB, CNR = 30dB.

4.5 Concluding Remarks

In this chapter, three CFAR detection algorithms using a MIMO random array were considered. The first detector considered was the well-known adaptive beamformer. The statistics of the ABF were reviewed, it was then shown that since the ABF does not remove the contributions of detected targets it suffers from the high sidelobes of the MIMO random array. This means that in the presence of a target, the ABF is no longer a CFAR detector.

The second CFAR detector, is the proposed MP-CFAR algorithm. Similar to the MP-STAP algorithm presented in the previous chapter, the MP-CFAR relies on the sparsity of the targets which allows one to cope with the high sidelobes of the random array while taking advantage of the high resolution of the random array. Critically however, the MP-CFAR algorithm does not assume any knowledge of the number of targets. Instead, the MP-CFAR localizes the first target by finding the whitened steering vector that has the largest projection with the whitened data. The target is then tested by the proposed CFAR detector, if the target passes the test, the whitened steering vectors are modified to remove the contribution from that target. Subsequent targets are found in a similar fashion using the modified whitened steering vectors and are tested using the CFAR detector. The process continues until a target fails the detection test. This iterative process bypasses the need to know any knowledge on the number of targets. In contrast, recall that the MP-STAP algorithm first localizes $\overline{K}$ targets before performing detection and hence required knowledge of $\overline{K}$, where $\overline{K}$ is the upper bound on the number of targets. The MP-CFAR avoids dealing with the high sidelobes of a random array by eliminating the contributions from target that has been detected. The MP-CFAR has two major advantages over the MP-STAP detection algorithm. Unlike MP-STAP, MP-CFAR does not require any information on the number of targets, in addition, the statistics of MP-CFAR can be analyzed, hence a CFAR radar can be designed using MP-CFAR .

The MBMP-CFAR generalizes the MP-CFAR algorithm and considers multiple candidates for the first target as opposed to just one candidate as in MP-CFAR. MBMP-CFAR also considers multiple candidates for the second and subsequent targets. This generalization provides a higher probability of correct recovery than the MP algorithm, which leads to an improved detection performance. Numerical results confirms that MBMP-CFAR improved the detection performance of the radar when multiple targets exist on the angle-Doppler map.

CHAPTER 5

COMPUTATIONAL COMPLEXITY

In the previous chapter, the MP-CFAR and MBMP-CFAR algorithms were introduced and was shown to improve the radar's performance in terms of the detection and false alarm probabilities. Although a significant improvement was observed, it is unclear how computationally intensive the MP-CFAR and MBMP-CFAR algorithms are. Since GMTI radar is potentially ran in real time, these algorithm cannot be too computationally intensive.

In this chapter, the computational complexity of the MP-CFAR and MBMP-CFAR is analyzed and compared to the beamformer. It will be shown that MP-CFAR is roughly k times more computationally intensive than the beamformer and MBMP-CFAR is roughly $N_D(k-1)$ times more computationally intensive than the beamformer where k is the number of targets detected by MP-CFAR and $N_D(k-1)$ is the number of localization solutions with at most $k-1$ targets that MBMP-CFAR generates. Since k is assumed to be small this increase in computational complexity is a modest increase considering the significant increase in performance shown in the previous chapter.

In addition, in this chapter off-grid targets are also considered. To handle the detection of off-grid targets a grid refinement procedure such as the one used in [41] is presented. By combining the MP-CFAR and the MBMP-CFAR algorithms with a grid refinement procedure the Grid-refined MP-CFAR and the Grid-refined MBMP-CFAR algorithms are developed respectively. The computational complexity of both Grid-refined MP-CFAR and Grid-refined MBMP-CFAR algorithms are considered. It will be shown that the Grid-refined MP-CFAR algorithm is roughly k^2 times

more computationally complex than the ABF and the Grid-refined MBMP-CFAR is roughly $N_D^2(k)$ times more computationally more complex than the ABF.

5.1 Beamforming

In this section, the computational complexity of the adaptive beamformer is reviewed. The computational complexity of the beamformer will serve as a benchmark for comparison with MBMP-CFAR. Recall that the beamformer digitally steers an array for all points on an angle-Doppler map, and calculates the output of the AMF test statistic for each resolution cell. For convenience the AMF test statistic for the i-th resolution cell is reproduced

$$T_i = \frac{|\mathbf{a}_i^H \hat{\mathbf{R}}^{-1} \mathbf{y}|^2}{\mathbf{a}_i^H \hat{\mathbf{R}}^{-1} \mathbf{a}_i} \geq \gamma. \tag{5.1}$$

Here, $\mathbf{a}_i$ is the $N \times 1$ steering vector of the i-th resolution cell, $\mathbf{y}$ is the $N \times 1$ measurement vector, γ is a threshold parameter set from false alarm considerations, and $\hat{\mathbf{R}}$ is the $N \times N$ scaled estimate of the covariance matrix. Let $\mathbf{w}_i = \hat{\mathbf{R}}^{-1}\mathbf{a}_i$, then (5.1) can be rewritten as

$$T_i = \frac{|\mathbf{w}_i^H \mathbf{y}|^2}{\mathbf{a}_i^H \mathbf{w}} \geq \gamma. \tag{5.2}$$

To obtain the number of flops required to compute the numerator, one can first compute how many flops are required to obtain $\mathbf{w}_i$ and then how many flops are required to perform the two inner products $|\mathbf{w}_i^H \mathbf{y}|^2$ and $\mathbf{a}_i^H \mathbf{w}$. The vector $\mathbf{w}$ is obtained by performing a product between a $N \times N$ matrix and a $N \times 1$ vector and requires $\mathcal{O}(N^2)$ flops. Both the numerator and denominator of (5.2) then becomes an inner product between two $N \times 1$ vectors which requires $\mathcal{O}(N)$ flops. Therefore, the computation of a single resolution cell requires $\mathcal{O}(N^2 + N) \approx \mathcal{O}(N^2)$ flops. If G

resolution cells are being tested then $\mathcal{O}(N^2G)$ flops are required to compute the test statistic for the entire angle-Doppler map.

5.2 CFAR Compressed Sensing Radar

Recall from the previous chapter, CS radar solves the optimization problem

$$\min_{\mathbf{x}} \|\mathbf{z} - \mathbf{B}\mathbf{x}\|_2^2 \text{ subject to } \|\mathbf{x}\|_0 \leq K \tag{5.3}$$

Where $\mathbf{z} = \widehat{\mathbf{R}}^{-1/2}\mathbf{y}$ and $\mathbf{B} = \widehat{\mathbf{R}}^{-1/2}\mathbf{A}$ is the whitened data vector and the whitened set of steering vectors respectively. The MP-CFAR and the MBMP-CFAR algorithms were proposed to find an approximate solution to the above optimization problem. In this section, the computational complexity of both the MP-CFAR and MBMP-CFAR is analyzed.

5.2.1 MP-CFAR

Recall that the inputs into the MP-CFAR are the measurement vector $\mathbf{y}$, the matrix of steering vectors $\mathbf{A}$, the estimate of the covariance matrix $\hat{\mathbf{R}}$, and a threshold parameter γ. The MP-CFAR begins by computing the matrix of whitened steering vectors $\mathbf{B} = \hat{\mathbf{R}}^{-1/2}\mathbf{A}$ and the whitened data $\mathbf{z} = \hat{\mathbf{R}}^{-1/2}\mathbf{y}$. Computing the whitened the $N \times 1$ data vector requires $\mathcal{O}(N^2)$ flops. Similarly, computing a whitened steering vector also requires $\mathcal{O}(N^2)$ flops and whitening G steering vectors requires $\mathcal{O}(N^2G)$ flops. MP-CFAR then searches for the index of the whitened steering vector $\mathbf{b}_j$ that has the largest projection with the whitened data $\mathbf{z}$.

$$m_1 = \max_j \frac{|\mathbf{b}_j^H \mathbf{z}|^2}{\mathbf{b}_j^H \mathbf{b}_j} \tag{5.4}$$

for $j = 1, \ldots, G$. Computing $|\mathbf{b}_j^H \mathbf{z}|^2 / \mathbf{b}_j^H \mathbf{b}_j$ requires $\mathcal{O}(N)$ flops. If G inner products are performed, $\mathcal{O}(NG)$ are required to compute the inner product for all G steering

vectors. Recall that the index m_1 localizes the target in the angle-Doppler domains. It then tests the m_1-th resolution cell using the CFAR detector in Chapter 3.2 for the presence of a target. For the first target, the test statistic was shown to be the same as (5.1) and requires $\mathcal{O}(N^2)$ operations. If the detection test fails, the algorithm terminates, otherwise the algorithm accepts m_1 as a target and continues to localize the next target.

From the above argument, to detect one target with MP-CFAR, one needs to perform whitening of the steering vectors which requires $\mathcal{O}(N^2G)$ flops, whitening the data vector which requires $\mathcal{O}(N^2)$ flops, localizing a target requires $\mathcal{O}(NG)$ flops and finally, performing the detection test requires $\mathcal{O}(N^2)$ flops. Since the number of resolution cells G is assumed to be much larger than the number measurements N, the computational complexity is dominated by $\mathcal{O}(N^2G)$. Therefore, the detecting the first target using MP-CFAR requires approximately $\mathcal{O}(N^2G)$ flops.

The computational complexity for the localization of the k-th target using MP-CFAR is now discussed. Let S_{k-1} be the set of indicies of columns of $\mathbf{B}$ associated with detected targets. Then, MP-CFAR computes the $N \times N$ orthogonal projection matrix orthogonal to the detected targets reproduced here for convenience

$$\mathbf{P}^{\perp}_{\mathbf{B}_{S_{k-1}}} = \mathbf{I} - \mathbf{B}_{S_{k-1}} \left(\mathbf{B}^{H}_{S_{k-1}} \mathbf{B}_{S_{k-1}} \right)^{-1} \mathbf{B}^{H}_{S_{k-1}}. \tag{5.5}$$

Computing (5.5) directly requires about $\mathcal{O}(11N^3)$ flops [79] however, a faster alternative way to compute (5.5) is through the use the modified Gram-Schmidt method, which requires $\mathcal{O}(2(k-1)N^2)$ flops instead. MP-CFAR then uses this projection matrix to remove the contributions of the target from the whitened steering vectors. The modified steering vectors that are orthogonal to the detected targets are formed $\omega_j = \mathbf{P}^{\perp}_{\mathbf{B}_{S_{k-1}}} \mathbf{b}_j / \| \mathbf{P}^{\perp}_{\mathbf{B}_{S_{k-1}}} \mathbf{b}_j \|_2$ for all $j \notin S_{k-1}$.

Computing a normalized steering vector orthogonal to the detected targets also requires $\mathcal{O}(N^2)$ flops. Then, computing $G-k+1$ normalized steering vectors orthogonal to the detected targets requires $\mathcal{O}((G-k+1)N^2) \approx \mathcal{O}(GN^2)$ flops for $k \ll G$. The k-th target is then localized

$$m_k = \max_j \ |\omega_j^H \mathbf{z}|^2 \tag{5.6}$$

which requires $\mathcal{O}(GN)$ flops. Finally, the detection test for the k-th target discussed in Chapter 3 is given by

$$T_{m_k}(m_k, S_k) = \frac{|\mathbf{f}_{m_k}^H \mathbf{z}|^2}{\mathbf{f}_{m_k}^H \mathbf{f}_{m_k}} \geq \gamma \tag{5.7}$$

where $S_k = S_{k-1} \bigcup m_k$ and $\mathbf{f}_{m_k} = \mathbf{P}^{\perp}_{\mathbf{B}_{S_k \setminus m_k}} \mathbf{b}_{m_k}$. To obtain the 'cleaned' steering vector $\mathbf{f}_{m_k}$ one must perform the product between the $N \times N$ matrix $\mathbf{P}^{\perp}_{\mathbf{B}_{S_k \setminus m_k}}$ and the $N \times 1$ steering vector $\mathbf{b}_{m_k}$ which requires $\mathcal{O}(N^2)$ flops. Then, obtaining all k 'cleaned' steering vectors requires $\mathcal{O}(kN^2)$ flops. The test statistic (5.7) is a ratio of two inner products of $N \times 1$ vectors requiring $\mathcal{O}(N)$ flops each and therefore computing the test statistic for a single target requires $\mathcal{O}(N)$ flops. Computing the test statistic for all k targets require $\mathcal{O}(kN)$ flops.

To recap, to localize the k-th target with MP-CFAR, one needs to first compute the orthogonal projection matrix $\mathbf{P}^{\perp}_{\mathbf{B}_{S_{k-1}}}$ which requires $\mathcal{O}(2(k-1)N^2)$ flops. MP-CFAR then projects the whitened steering vectors away from the detected targets which requires $\mathcal{O}(N^2G)$ flops. Localizing the k-th target requires $\mathcal{O}(N)$ flops and finally, computing the detection test for all k targets requires $\mathcal{O}(kN^2)$ flops. Again, the computational complexity of localizing the k-th target is dominated by $\mathcal{O}(N^2G)$. Therefore, detecting the k-th target using MP-CFAR requires $\mathcal{O}(N^2G)$ flops. Since it takes $\mathcal{O}(GN^2)$ to detect a target it requires $\mathcal{O}(kGN^2)$ flops to detect k targets.

Comparing the computational complexity of MP-CFAR to the adaptive beamformer it is seen that the MP-CFAR is k times more computational complex than the adaptive beamformer. It is noted that the computational complexity of MP-CFAR scales linearly with the number of targets. Since the number of targets is assumed to be sparse k is relatively small value and the additional computational burden on the processor using MP-CFAR is a modest increase.

5.2.2 MBMP-CFAR

The computational complexity of implementing the MBMP-CFAR algorithm is now analyzed. Recall that the strategy of the MBMP-CFAR algorithm is to generate multiple candidates for the location of the first target. Each candidate target then serves as a seed to the localization and detection of subsequent targets. When the process is completed, a metric is used to select the set of targets that provide the best fit to the data. The inputs into the MBMP-CFAR are the measurement vector $\mathbf{y}$, the matrix of steering vectors $\mathbf{A}$, the estimate of the covariance matrix $\hat{\mathbf{R}}$, a set of G positive integers D, and a threshold parameter γ. MBMP-CFAR begins by initializing a node with an empty set, it then computes the matrix of whitened steering vectors $\mathbf{B} = \hat{\mathbf{R}}^{-1/2}\mathbf{A}$ and the whitened data $\mathbf{z} = \hat{\mathbf{R}}^{-1/2}\mathbf{z}$. From the previous section, computing the whitened data $\mathbf{z}$ requires $\mathcal{O}(N^2)$ and whitening all G steering vectors requires $\mathcal{O}(GN^2)$ flops. MBMP-CFAR then proceeds to find the d_1 indicies $m_1, m_2, \ldots, m_{d_1}$, that produce the d_1 largest projections of steering vectors $\mathbf{b}_j$ on the whitened data $\mathbf{z}$. Specifically, the resolution cell index that localizes the first branch of the first target is found from

$$m_1^{(1)} = \arg\max_j \frac{|\mathbf{b}_j^H \mathbf{z}|^2}{\mathbf{b}_j^H \mathbf{b}_j} \tag{5.8}$$

for $j = 1, 2, \ldots, G$. The i-th branch of the first target, $1 \leq i \leq d_1$, is found from

$$m_1^{(i)} = \arg \max_{j \notin m_1, \ldots m_{i-1}} \frac{|\mathbf{b}_j^H \mathbf{z}|^2}{\mathbf{b}_j^H \mathbf{b}_j}. \tag{5.9}$$

All d_1 branches can be obtained by computing $|\mathbf{b}_j^H \mathbf{z}|^2 / \mathbf{b}_j^H \mathbf{b}_j$ for $j = 1, 2, \ldots, G$. From the previous section, computing the inner product $|\mathbf{b}_j^H \mathbf{z}|^2 / \mathbf{b}_j^H \mathbf{b}_j$ requires $\mathcal{O}(N)$ flops. If G inner products are performed, $\mathcal{O}(NG)$ are required to compute the inner product for all G steering vectors.

MBMP-CFAR then tests the $m_1^{(1)}$-th resolution cell for the presence of a target. From the previous section, computing the test statistic for a single target requires $\mathcal{O}(N^2)$ flops. If the test statistic does not exceed the threshold γ, MBMP-CFAR declares that no targets are present and the algorithm terminates. Otherwise, MBMP-CFAR updates d_1 target sets as follows $S_1^{(i)} = \{m_1^{(i)}\}$ for $1 \leq i \leq d_1$.

To detect the presence of a single target with MBMP-CFAR, one needs to perform whitening of the steering vectors which requires $\mathcal{O}(N^2 G)$ flops, whitening the data vector which requires $\mathcal{O}(N^2)$ flops, localizing a target which requires $\mathcal{O}(NG)$ flops, and finally, performing the detection test requires $\mathcal{O}(N^2)$ flops. Therefore, detecting a single target using MBMP-CFAR requires approximately $\mathcal{O}(N^2 G)$ flops.

The computational complexity for the detection of the k-th target using MBMP-CFAR is now discussed. Let the $S_{k-1}^{(i_1,\ldots,i_{k-1})}$ be a localization solution generated by MBMP-CFAR. MBMP-CFAR then computes the orthogonal projection matrix $\mathbf{P}^{\perp}_{\mathbf{B}_{S_{k-1}^{(i_1,\ldots,i_{k-1})}}}$ which requires $\mathcal{O}(2(k-1)N^2)$ flops. MBMP-CFAR then uses this matrix to determine a new set of normalized steering vectors orthogonal to the detected targets $\mathbf{w}_j = \mathbf{P}^{\perp}_{\mathbf{B}_{S_{k-1}^{(i_1,\ldots,i_{k-1})}}} \mathbf{b}_j$ for $j \notin \mathbf{B}_{S_{k-1}^{(i_1,\ldots,i_{k-1})}}$. Computing the steering vectors orthogonal to the detected targets $\mathbf{w}_i$ for $i \notin S_j$ requires $\mathcal{O}((G-k+1)N^2) \approx \mathcal{O}(GN^2)$ flops. The algorithm then proceeds to find the d_k indicies $i_1, i_2, \ldots, i_{d_k}$ from

$$m_k^{i_1,\ldots,i_{k-1}} = \arg \max_{j \notin m_1,\ldots,m_{k-1}}$$

which requires $\mathcal{O}(GN)$ flops to generate d_k localization solutions. This process is repeated for all $D_{k-1} = \prod_{i=1}^{k-1} d_i$ localization solutions with $k-1$ targets. MBMP-CFAR then computes the path that minimizes the residual

$$(i_1, i_2, ..., i_k) = \arg \min_{(j_1,...,j_k)} R^{(j_1,...,j_k)}$$

where

$$R^{(i_1,...,i_k)} = \left\| \mathbf{P}^{\perp}_{\mathbf{B}_{S_k^{(i_1,...,i_k)}}} \mathbf{z} \right\|_2^2 .$$

Computing the residual for a single path requires one to compute the 2-norm of a matrix-vector product. The matrix-vector product requires $\mathcal{O}(N^2)$ and computing the 2-norm requires $\mathcal{O}(N)$ flops, therefore computing the residual for a single path requires $\mathcal{O}(N^2)$ flops. Computing the residual for all D_k paths therefore requires $\mathcal{O}(D_k N^2)$ flops. The path that minimizes the residual is then tested for the presence of a target. From the previous section, it requires $\mathcal{O}(kN^2)$ flops to perform the detection test for all k targets.

To recap, to detect the k-th target with MBMP-CFAR, for every localization solution generated by MBMP-CFAR with $k-1$ targets, MBMP-CFAR computes an orthogonal projection matrix which requires $\mathcal{O}(2(k-1)N^2)$ flops for each localization solution. Therefore, $\mathcal{O}(D_{k-1}2(k-1)N^2)$ flops are required to compute the orthogonal projection matrix for all D_{k-1} localization solutions. MBMP-CFAR then projects the steering vectors orthogonally to the detected targets which requires $\mathcal{O}(GN^2)$ flops per localization solution. Therefore, $\mathcal{O}(D_{k-1}GN^2)$ flops are required to project the steering vectors orthogonally to the detected targets for all D_{k-1} localization solutions. Localizing the k-th target requires $\mathcal{O}(D_{k-1}GN)$ flops and finally, computing the test statistic requires $\mathcal{O}(kN^2)$ flops. The computational complexity of detecting the k-th target is dominated by step where MBMP-CFAR modifies the steering

vectors which requires $\mathcal{O}(D_{k-1}N^2G)$ flops, hence detecting the k-th target with MBMP-CFAR requires $\mathcal{O}(D_{k-1}N^2G)$ flops. Therefore, detecting all k targets requires $\mathcal{O}(N_D(k-1)N^2G)$ flops, where

$$N_D(k-1) = \sum_{l=1}^{k-1} D_i. \tag{5.10}$$

Notice that D_l is the number of localization solutions with l targets. Hence, (5.10) represents the total number of localization solutions obtained by MBMP-CFAR with at most $k-1$ targets. Comparing the computational complexity of MBMP-CFAR to the adaptive beamformer it is seen that the MBMP-CFAR is $N_D(k-1)$ times more computational complex than the adaptive beamformer. Therefore, the computational complexity of MBMP-CFAR scales linearly with the number of localization solutions obtained. This points to a trade off between computational complexity on one hand, and the probability of correct recovery on the other. Notice that when $D_i = 1$ for all i the MBMP-CFAR simplifies to the MP-CFAR and requires the same number of flops.

5.3 Grid Refinement Techniques

So far in this dissertation, it was assumed that all the targets comply with the discretized grid of angle-Doppler points. In reality, targets almost never comply with a grid of discretized points and targets often lie off the grid regardless how fine the granularity of the grid becomes. When targets do not comply with the discrete grid of angle-Doppler points it was shown that the performance of both BP and MP based algorithms may degrade significantly [59, 61]. In radars that use CS, these degradations present itself as a loss in SNR and as a significant increase in the probability of false alarm.

Numerous techniques have been proposed in literature [62]–[66] to mitigate the effects of off-grid targets. The most straightforward method to handle off-grid targets is to simply increase the number of grid points sampled on the angle-Doppler map. This method, although simple, increases the computational complexity of MP algorithms since the computational complexity increases linearly with the number of grid points G additionally, the use of very fine grids may lead to numerical instability issues. In [62, 65, 66] the authors propose approximate the nonconvex penalty term $\|\mathbf{x}\|_0$ in (5.3) with the convex penalty term $\|\mathbf{x}\|_{\mathcal{A}}$ where $\|\mathbf{x}\|_{\mathcal{A}}$ refers to the *atomic norm* (more details on the atomic norm can be found in [69]). The resulting optimization problem is convex and can be solved by a convex solver in polynomial time. Similar to BP, the computation time required to solve the optimization problem proposed in [62] is too large for radar applications. The authors in [63] proposed a matrix completion algorithm to mitigate the effects of off-grid targets. However, the authors noted that the matrix completion algorithm requires the same computation time as the optimization problem in [62] and therefore impractical for radar applications.

In this dissertation, a simple grid refinement technique is used to handle off-grid targets. Grid refinement was most notably used in [41] and utilizes a very simple heuristic. The motivation behind grid refinement is intuitive: if the number of grid points G is chosen such that the grid spacing matches the requirement for target's location accuracy δ, and if δ is small, then G becomes large. Instead, the grid-refined starts with a coarse grid with spacing $\delta_0 > \delta$, which generates a grid of $G_0 < G$ points. MP or MBMP are ran on this coarse grid to obtain an initial estimate of target locations, the grid is then refined locally for the grid points that correspond to target locations and the remaining grid points are discarded. The algorithm that utilizes MP to obtain an initial estimate of target locations is referred to as Grid-refined MP-CFAR. Similarly, the algorithm that utilizes MBMP to obtain an initial estimate of target locations is referred to as Grid-refined MBMP-CFAR. In

this section the Grid-refined MP-CFAR and Grid-refined MBMP-CFAR is detailed and the computational complexity of running both algorithms is discussed.

5.3.1 Grid-refined MP-CFAR

Grid-refined MP-CFAR can be thought of as a three stage algorithm. In the first stage, the algorithm searches for an initial estimate of k target locations using MP, where k is the iteration counter for the algorithm. In the second stage, Grid-refined MP-CFAR refines the grid locally around the k target locations obtained in the first stage and generates a new finer grid. Finally, in the last stage MP-CFAR is ran using the new refined grid. If MP-CFAR declares that at least k targets are present on the new refined grid, the algorithm increments k by one and reiterates the process, otherwise, the algorithm terminates and outputs the set S_{k-1}, where S_{k-1} is the set of detected targets on the $(k-1)$-th iteration. A block diagram of MP-CFAR with the grid refinement procedure is shown in Figure 5.1

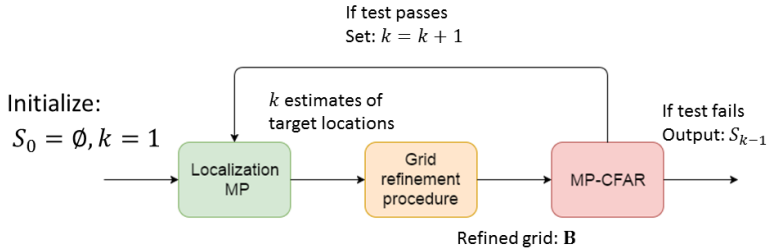

Figure 5.1 Block diagram of MP-CFAR with a grid refinement procedure.

The inputs into Grid-refined MP-CFAR are the measurement vector $\mathbf{y}$, the matrix of steering vectors $\mathbf{A}$, the estimate of the covariance matrix $\hat{\mathbf{R}}$, a threshold parameter γ, and a desired accuracy δ. Let the number of initial grid points be G and let the spacing between grid point be given by δ_0 the algorithm begins by setting a counter k to $k = 1$. The first candidate target is localized by the index m_1 of the vector $\mathbf{b}_j$ that has the largest data projection,

$$m_1 = \arg\max_j \frac{|\mathbf{b}_j^H \mathbf{z}|^2}{\mathbf{b}_j^H \mathbf{b}_j} \tag{5.11}$$

for $j = 1, ..., G$. The index m_1 becomes the initial estimate of the target in the angle-Doppler domains. The estimate of the k-th target location is now described given that $k-1$ target locations have been determined. Let the matrix $\mathbf{B}$ be formed with the columns $\mathbf{b}_j$. Let S_{k-1} be the set of indices of columns of $\mathbf{B}$ associated with detected targets, and let $\mathbf{B}_{S_{k-1}}$ be the matrix formed by the columns indexed by S_{k-1}. The projection matrix orthogonal to the detected targets is given by $\mathbf{P}^{\perp}_{\mathbf{B}_{S_{k-1}}} = \mathbf{I} - \mathbf{B}_{S_{k-1}} \left(\mathbf{B}^H_{S_{k-1}} \mathbf{B}_{S_{k-1}} \right)^{-1} \mathbf{B}_{S_{k-1}}$. The steering vectors orthogonal to the detected targets are formed as follows: $\mathbf{w}_j = \mathbf{P}^{\perp}_{\mathbf{B}_{S_{k-1}}} \mathbf{b}_j$, for all $j \notin S_{k-1}$. The k-th target is localized according to

$$m_k = \arg\max_j \frac{|\mathbf{w}_j^H \mathbf{z}|^2}{\mathbf{w}_j^H \mathbf{w}_j}. \tag{5.12}$$

Once all k estimates of target locations is obtained, Grid-refined MP-CFAR proceeds to refine the grid locally around all k resolution cells. Let m_l be one of the resolution cells obtained in the first stage of Grid-refined MP-CFAR and let the resolution cell be associated with the spatial frequency u_l and Doppler f_l. Then, all angle-Doppler pairs associated to spatial frequencies

$$[u_l - \delta_0,\ u_l - \delta_0 + \delta,\ \ldots, u_l + \delta_0 - \delta,\ u_l + \delta_0]$$

and Doppler

$$[f_l - \delta_0,\ f_l - \delta_0 + \delta,\ \ldots, f_l + \delta_0 - \delta,\ f_l + \delta_0]$$

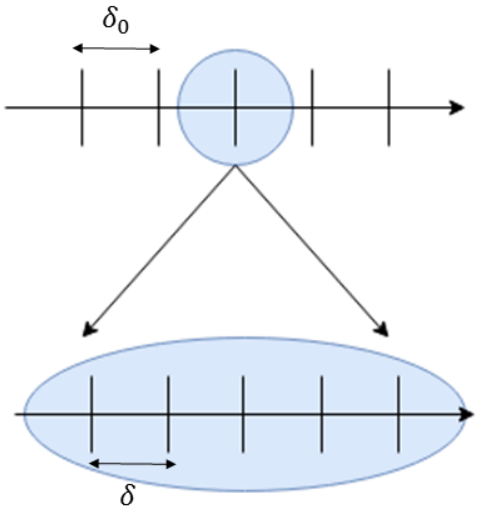

Figure 5.2 Illustration of the grid refinement procedure in one dimension.

are used to form a new grid. Note that $(2\Delta + 1)^2$ where $\Delta = \delta_0/\delta$ points are formed for the new grid. This process is repeated for all k grid points generating a new grid with $G_k = k(2\Delta + 1)^2$ grid points. Once the new grid is constructed, Grid-refined MP-CFAR uses the newly formed grid as an input into the MP-CFAR algorithm. If MP-CFAR localizes and detects k targets, Grid-refined MP-CFAR increments the counter k by one and reiterates the process. This continues until MP-CFAR fails to detect at least k targets. The refinement procedure in one dimension is illustrated in Figure 5.2

The computational complexity of the Grid-refined MP-CFAR is now analyzed. First, consider the computational complexity of the k-th iteration of the Grid-refined MP-CFAR. From the previous section, the localization of k targets requires $\mathcal{O}(kGN^2)$ flops. A new grid is then generated, with G_k grid points and MP-CFAR is ran using the new grid. From the previous section, $\mathcal{O}(kG_kN^2)$ flops are required to execute MP-CFAR with G_k grid points. Therefore, the computational complexity of the k-th iteration of Grid-refined MP-CFAR is given by

$$\mathcal{O}(kGN^2 + G_kN^2) = \mathcal{O}(kN^2(G + (2\Delta + 1)^2))$$

If the desired accuracy is chosen such that $G \approx (2\Delta+1)^2$ the above expression can be simplified to $\mathcal{O}(kGN^2)$. Therefore, the computational complexity of Grid-refined MP-CFAR for the k-th iteration can be approximated as $\mathcal{O}(kGN^2)$. The computational complexity required to run k iterations of Grid-refined MP-CFAR is then given by

$$\begin{aligned}\sum_{m=1}^{k} \mathcal{O}(mN^2G) &= \mathcal{O}(\frac{k(k+1)}{2}N^2G) \\ &\approx \mathcal{O}(k^2N^2G).\end{aligned}$$

Notice that the computational complexity Grid-refined MP-CFAR is about k times more computationally expensive than the MP-CFAR. Since the number of targets k is small this is a modest increase in computational complexity.

5.3.2 Grid-refined MBMP-CFAR

The Grid-refined MP-CFAR algorithm obtains an estimate of the first target according to (5.11), namely, finds the column of the whitened measurement matrix with the largest projection on the whitened data $\mathbf{z}$. As with MP-CFAR, the performance of Grid-refined MP-CFAR is negatively impacted if Grid-refined MP-CFAR localizes the target in the wrong resolution cell since localizing subsequent candidate targets depends on the location of the first target. A more robust approach is to find multiple candidate targets for location of the first target.

To this end, the MP algorithm is replaced with the MBMP algorithm to obtain an initial estimate of target locations. At the end of the MBMP algorithm, $N_D(k)$ localization solutions each with k targets is obtained. Grid-refined MBMP-CFAR then refines the grid locally around all $kN_D(k)$ resolution cells obtained by MBMP in

the same fashion as the Grid-refined MP-CFAR. Once the new grid is generated, MBMP-CFAR uses the newly formed grid as an input to the MBMP-CFAR algorithm. If MBMP-CFAR localizes and detects k targets, Grid-refined MBMP-CFAR increments the counter k by one and reiterates the process. This continues until MBMP-CFAR fails to detect at least k targets.

The computational complexity of the Grid-refined MBMP-CFAR is now analyzed. First, consider the computational complexity of the k-th iteration of the Grid-refined MBMP-CFAR. From the previous section, the localization of k targets requires $\mathcal{O}(N_D(k-1)GN^2)$ flops. A new grid is then generated, with $G_k = kN_D(k)(2\Delta+1)^2$ grid points and MBMP-CFAR is ran using the new grid. From the previous section, $\mathcal{O}(N_D(k-1)G_kN^2)$ flops are required to execute MBMP-CFAR with G_k grid points. Therefore, the computational complexity of the k-th iteration of Grid-refined MBMP-CFAR is given by

$$\mathcal{O}(N_D(k-1)GN^2 + N_D(k-1)G_kN^2) = \mathcal{O}(N_D(k-1)N^2(G+G_k)).$$

If the desired accuracy is chosen such that $G \approx (2\Delta+1)^2$ the above expression can be simplified to $\mathcal{O}(N_D(k-1)G_kN^2)$. Therefore, the computational complexity of Grid-refined MP-CFAR for the k-th iteration can be approximated as

$$\mathcal{O}(N_D(k-1)G_kN^2) \approx \mathcal{O}(N_D^2(k-1)kGN^2).$$

The computational complexity required to run k iterations of Grid-refined MP-CFAR is then given by

$$\sum_{m=1}^{k-1} \mathcal{O}(N_D^2(m)kGN^2)$$

From the above equation, the computational complexity of the Grid-refined MBMP-CFAR depends on the square of the number of localization solutions obtained by MBMP-CFAR. Hence, again pointing to a trade off between computational complexity on one hand, and the probability of correct recovery on the other.

5.4 Numerical Results

In this section, numerical examples are presented to compare the performance and computational complexity of ABF, Grid-refined MP-CFAR and the Grid-refined MBMP-CFAR algorithms. For all algorithms, the number of receive elements is $N_r = 4$, the number of transmit elements is $N_t = 2$, and the number of coherent pulses is given by $N_p = 16$ and the array length is given by $Z = Z_t + Z_r = 8\lambda$. The SNR of the target is set to 20 dB and the CNR is set to 30 dB. The number of training samples used to estimate the covariance matrix for the random array is $L = 2N$. The number of resolution cells on the angle-Doppler map is given by $G = (2Z + 1)^2 = 289$. For all figures, a random realization of an array is drawn and remains fixed throughout the Monte Carlo simulations. Let S_t be the true set of resolution cells that contain targets, and let $\hat{S}$ be the set of resolution cells found by a detector to have targets. Let $(\hat{u}, \hat{f})$ be the estimate of a target's parameters where the true parameters of the target is given by the angle-Doppler pair (u, f). Then, the RMSE is defined as RMSE $= \sqrt{(u - \hat{u})^2 + (f - \hat{f}^2)}$. A target is considered detected correctly if RMSE $\leq \sqrt{1/2Z^2}$.

In Figure 5.3 the RMSE is plotted as a function of the desired accuracy for the MP-CFAR algorithm. From the figure, as expected the RMSE is seen to decrease as the spacing between grid points decreases. Once the spacing between grid points decrease to about $1/8Z$ (recall that $1/Z$ is the approximate beamwidth) the RMSE levels off and further refinement of the grid does not decrease the RMSE and improvements to the RMSE cannot be made due to the presence of noise. From

the figure, a refinement factor of about $\Delta \geq 8$ achieves a RMSE of about 0.025. Note that $\Delta = 8$ corresponds to generating a new grid of $G_k = (2\Delta + 1)^2 = G$ and satisfies the assumption that $G \approx G_k$ that was made in this chapter.

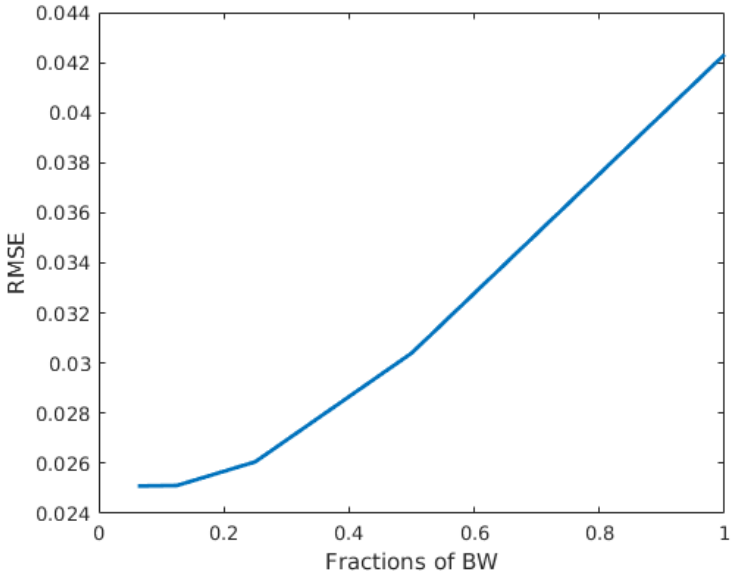

Figure 5.3 RMSE vs the grid spacing of the refined grid.

In Figure 5.4, the ROC curves for the ABF and MP-CFAR are plotted when a target comply with the discretized grid of points. The target is placed at $(u = 0, f = 1/N_p)$, near the clutter ridge in the angle-Doppler map. In addition, the ROC for the Grid-refined MP-CFAR is also plotted. The refinement factor Δ is set to 8. The target is placed at $(u = \delta, f = 1/N_p + \delta)$ where δ is drawn from a uniform distribution $\delta \sim [0,\ 1/Z]$. From the figure, ABF again performs the worst since it cannot cope with the high sidelobes of the MIMO random array and MP-CFAR performs the best. The grid-refined MP-CFAR still outperforms the ABF but performs worse than the MP-CFAR when the target lies on the grid point. In particular, the false alarm probability of the Grid-refined MP-CFAR is about 3 times larger than the probability of false alarm experienced by MP-CFAR. This increase in the probability of false alarm is attributed to the fact that the target does not comply with the grid of

discretized points. With very high probability, the target will not comply with a grid of discretized points no matter how fine the grid becomes. Since the algorithm cannot pinpoint the exact location of the target on the angle-Doppler map, it cannot remove all of the target's contributions using successive interference cancellation. This causes a small amount of energy to still leak into the sidelobes and increase the probability of false alarm.

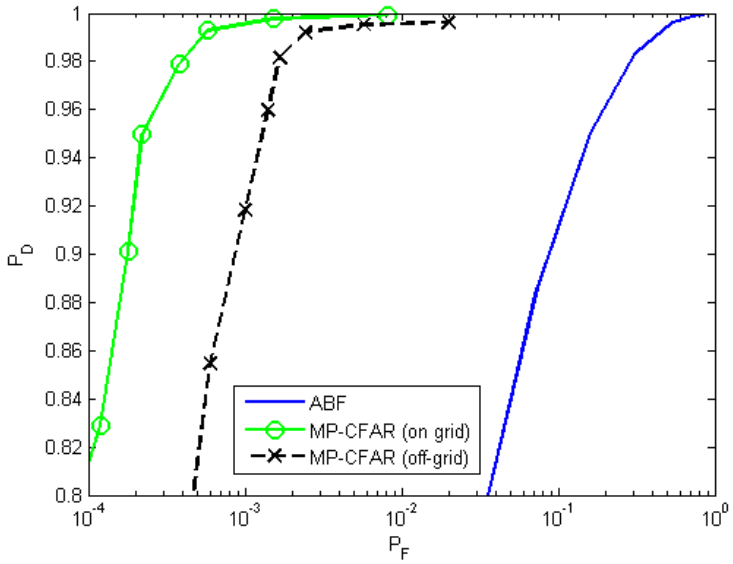

Figure 5.4 ROC curves for the ABF, MP-CFAR, and Grid-refined MP-CFAR algorithms. All algorithms utilize a MIMO random array with $N_t = 2$, $N_r = 4$, $N_p = 16$ with an array of size $Z = 8\lambda$. Parameters used: SNR= 20 dB, CNR= 30 dB, $K = 1$

In Figure 5.5 are shown the ROC curves for the ABF and MP-CFAR are plotted when targets comply with the discretized grid of points. Two targets with spatial frequency $u = 0$ are placed on the angle-Doppler map. Both targets are slowly moving, one target has a Doppler $1/N_p$ while the other has a Doppler of $-1/N_p$. In addition, the ROC for the Grid-refined MP-CFAR and Grid-refined MBMP-CFAR are also plotted. The targets are placed at $(u = \delta, f = 1/N_p + \delta)$ and $(u = -\delta, f = -1/N_p - \delta)$ where again, δ is drawn from a uniform distribution $\delta \sim [0,\ 1/Z]$. The refinement factor Δ is again set to 8. The number of branches used by Grid-refined MBMP-CFAR

is given by $D = \{5,\ 1, \ldots,\ 1\}$. From the figure, ABF again performs the worst out of the four methods and the MP-CFAR algorithm shows a significant performance gain. Also from the figure, it is seen that the Grid-refined MP-CFAR again experiences a higher false alarm rate than the MP-CFAR as expected. Interestingly, the Grid-refined MBMP-CFAR algorithm performs very similarly to the MP-CFAR algorithm even though the targets lies off the grid for the Grid-refined MBMP-CFAR and the targets lie on the grid for MP-CFAR. From Figure 5.4 it is clear that Grid-refined MBMP-CFAR will experience an increase in the probability of false alarm because it cannot completely remove the contributions of the target. However, since Grid-refined MBMP-CFAR has access to multiple target sets it has an improved probability of correct recover that is not available to MP-CFAR. This improved probability of correct recovery allows Grid-refined MBMP-CFAR to remain competitive to MP-CFAR even when the targets are off the grid.

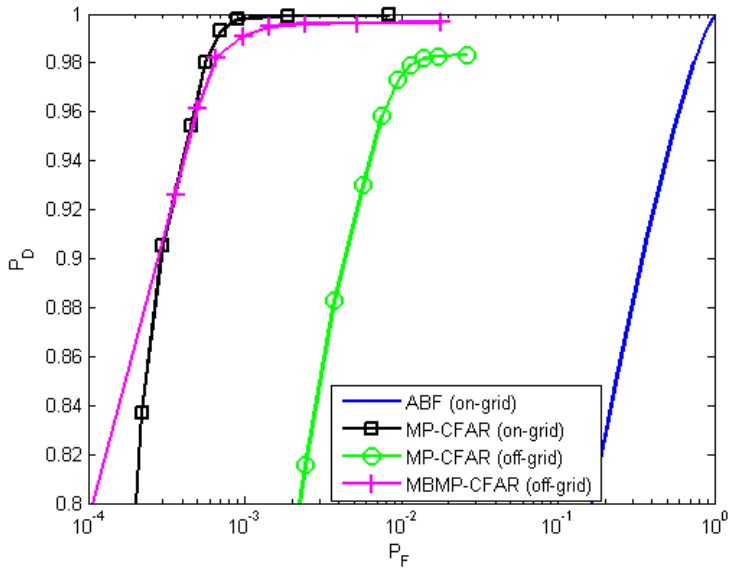

Figure 5.5 ROC curves for the ABF, MP-CFAR, Grid-refined MP-CFAR, and Grid-refined MBMP-CFAR algorithms. $D = \{5,\ 1 \ldots, 1\}$. All algorithms utilize a MIMO random array with $N_t = 2$, $N_r = 4$, $N_p = 16$ with an array of size $Z = 8\lambda$. Parameters used: SNR= 20 dB, CNR= 30 dB, $K = 2$

In Figure 5.6, the average runtime of the ABF, Grid-refined MP-CFAR and the Grid-refined MBMP-CFAR is plotted against the desired accuracy. The targets are placed at $(u = \delta, f = 1/N_p + \delta)$ and $(u = -\delta, f = -1/N_p - \delta)$ where again, δ is drawn from a uniform distribution $\delta \sim [0,\ 1/Z]$. The number of branched used by Grid-refined MBMP-CFAR is given by $D = \{5,\ 1, \ldots,\ 1\}$. From the figure, the ABF has the least average runtime, in addition since the ABF cannot discriminate targets within a beamwidth a refinement procedure is unnecessary and therefore not employed. Hence, the average runtime of the ABF in the figure remains constant. From the figure, the average runtime of the Grid-refined MP-CFAR increases as the spacing between grid points decreases. This is consistent, since a smaller grid spacing corresponds to a larger set of grid points in the refined grid. Note that for $\Delta = 8$ (or a grid spacing of $1/8Z$) the average runtime of the Grid-refined MP-CFAR is roughly 7 times longer than that of the beamformer. This increase in runtime is considered an acceptable increase in computational complexity compared to the performance gain Grid-refined MP-CFAR provides. Similarly to the Grid-refined MP-CFAR, the average runtime of the Grid-refined MBMP-CFAR is seen to increase as the spacing between grid points decreases. Also as expected, the runtime of Grid-refined MBMP-CFAR is higher than that of the MP-CFAR due to the extra localization solutions it generates.

5.5 Concluding Remarks

In this chapter, the computational complexity of the ABF, MP-CFAR and the MBMP-CFAR was analyzed. The computational complexity of the MP-CFAR algorithm was shown that roughly k times more computationally complex than the ABF where k is the number of targets detected by MP-CFAR. This slight increase in computational complexity is a modest increase considering the significant performance increase that was observed in the previous chapter. Similarly, MBMP-CFAR was

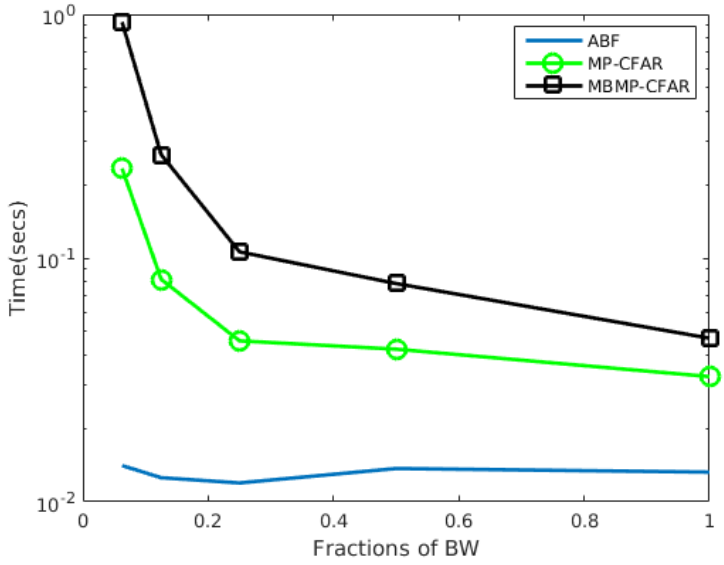

Figure 5.6 Average runtime time vs the grid spacing of the refined grid for the ABF, Grid-refined MP-CFAR, and Grid-refined MBMP-CFAR algorithms. The set D used by Grid-refined MBMP-CFAR is $D = \{5,\ 1\ldots,1\}$ All algorithms utilize a MIMO random array with $N_t = 2$, $N_r = 4$, $N_p = 16$ with an array of size $Z = 8\lambda$. Parameters used: SNR= 20 dB, CNR= 30 dB, $K = 2$

shown to be $N_D(k-1)$ times more computationally complex than the ABF where $N_D(k-1)$ is the number of localization solutions obtained by MBMP-CFAR that contains at most $k-1$ targets. This points to a trade off between computational complexity on one hand, and the performance of the radar on the other.

In addition, the detection of targets that lie off the grid of discretized set of angle-Doppler points were considered. To handle off-grid targets a grid refinement procedure was used with both MP-CFAR and MBMP-CFAR algorithms to develop the Grid-refined MP-CFAR and the Grid-refined MBMP-CFAR algorithms. Grid-refined MP-CFAR searches for an initial estimate of target locations using MP, it then refined the grid locally around the initial estimates and finally performs target detection on the new grid. Grid-refined MBMP-CFAR works similarly, but replaces the MP algorithm with MBMP and replaces the MP-CFAR with the MBMP-CFAR. The computational complexity of Grid-refined MP-CFAR and Grid-refined MBMP-

CFAR were also presented. It was shown that the Grid-refined MP-CFAR is k^2 times more computationally complex than the ABF. Since the number of targets is assumed to be small, this is still a relatively modest increase in computational complexity. The Grid-refined MBMP-CFAR was shown to be about $N_D^2(k)$ more computationally complex than the ABF. Note that the computational complexity depends on the number of localization solutions obtained by MBMP $N_D(k)$, hence again pointing to a design trade off between the performance of the algorithm and its computational complexity. Numerical examples show that grid refinement improves the estimation accuracy of the target on the angle-Doppler map the smaller the spacing between grid points are up to a point. When the spacing between grid points is smaller than about $1/8Z$, no improvement in the RMSE was seen. A small performance decrease was observed when detecting of off-grid targets with Grid-refined MP-CFAR and Grid-refinend MBMP-CFAR compared to when targets comply with the discretized grid of angle-Doppler points.

CHAPTER 6

CONCLUSIONS

In this dissertation, detection algorithms using concepts in space-time adaptive processing (STAP) were presented for the detection of potentially slow moving targets for ground moving target indicator (GMTI) radar using a large multiple-input multiple-output (MIMO) random array. The performance of two sparsity based detection algorithms, the matching pursuit - STAP (MP-STAP) and the multibranch matching pursuit STAP (MBMP-STAP) were presented. In addition, two sparsity based detection algorithms that maintains the desired constant false alarm rate (CFAR) property, matching pursuit - CFAR (MP-CFAR) and multibranch matching pursuit - CFAR (MBMP-CFAR) algorithms were also presented as improvements upon the MP-STAP and MBMP-STAP algorithms. The performance of both the MP-CFAR and MBMP-CFAR algorithms were analyzed in terms of the probability of detection and the probability of false alarm. An analysis of the computational complexity of both MP-CFAR and MBMP-CFAR were also presented. Lastly, to allow the detection algorithms to handle targets that lie off the grid of discretized angle-Doppler points a grid refinement procedure was added to MP-CFAR and MBMP-CFAR to develop the Grid-refined MP-CFAR and Grid-refined MBMP-CFAR algorithms respectively.

In Chapter 2, the signal model that was used throughout this dissertation was introduced. In addition, properties of the MIMO random array were presented. In particular, the array pattern of the MIMO random array was studied. In doing so, the statistics for the average sidelobe level and the average peak sidelobe level was derived. It was shown that the average sidelobe level is inversely proportional to the number of sensors in the array. The average peak sidelobe level is shown to be larger

than the average sidelobe level by a factor that scales logarithmically with the array aperture. The clutter response of MIMO random arrays were also presented. The resolution of the MIMO random array depends on the array aperture and therefore can support a lower minimum detectable velocity (MDV) than a uniform linear array (ULA) with the same number of elements. However, due to the spatial undersampling introduced by the MIMO random array, the rank of the clutter increases and the array must spend more degrees of freedom (DOF) canceling the clutter and therefore, must spend less DOF on providing gain for target detection compared to a ULA with the same number of elements.

In Chapter 3, the adaptive beamforming detection test is reviewed. In addition, two sparsity based detectors were developed, the MP-STAP and the MBMP-STAP algorithms. By using information on an upper bound on the number of targets, both sparsity based detectors obtain a set of resolution cells that are declared as target candidates. Since the algorithm obtains an upper bound on the number of targets there are likely to be false alarms present in the set of obtained sets of targets. To remove the false alarms from the solution, all target candidates are tested by a detector.

In Chapter 4, the statistics of the adaptive beamformer (ABF) were reviewed. It was shown that the ABF is unable to cope with the large sidelobes of a MIMO random array. New detection algorithms for airborne radar were proposed which combine the strengths of MIMO random arrays with the ability of sparsity based algorithms to handle undersampling effects. In particular, two sparsity-based CFAR detection algorithms were proposed, the matching pursuit-CFAR (MP-CFAR) and multibranch MP-CFAR (MBMP-CFAR), respectively. MP-CFAR consists of a target localization stage followed by a target detection stage. The target localization stage exploits the sparsity of the number of targets to cope with the undersampling of the MIMO random array. The target detection stage tests the localized targets obtained

from the first stage using a CFAR detector. MBMP-CFAR generalizes MP-CFAR by maintaining and updating multiple sets of candidate targets. The new detectors do not require *any* knowledge on the number of targets. The statistics of the new detectors were derived. As its name suggests, both MP-CFAR and MBMP-CFAR are CFAR detectors, in the sense that the statistics of the new detectors do not depend on the interference covariance matrix.

In Chapter 5, the computational complexity of the MP-CFAR and MBMP-CFAR is analyzed and compared to the beamformer. It was shown that MP-CFAR is roughly k times more computationally intensive than the beamformer and MBMP-CFAR is roughly $N_D(k-1)$ times more computationally intensive than the beamformer where k is the number of targets detected by MP-CFAR and $N_D(k-1)$ is the number of localization solutions with at most k targets that MBMP-CFAR generates. In addition, off-grid targets were considered, to handle off-grid targets a grid refinement algorithm was proposed. Although numerous sophisticated algorithms that handle the off-grid problem for CS algorithms have been proposed in literature, they often require the use of a convex solver and has high computational complexity. Grid refinement techniques as in [41], are less accurate than algorithms that make use of a convex solver, but require significantly less computational complexity allowing it to be ran in quasi-real time.

The main focus of this work was on the development of a sparsity based CFAR detector for GMTI radar. It was shown that the detection algorithms presented in this dissertation can maintain a desired false alarm probability even in the presence of a strong interferer. In addition, using grid-refinement techniques these algorithms are not constrained to a discretized grid of angle-Doppler points. The detection algorithms are also shown to competitive in computational complexity compared to the ABF while being able to provide a significant performance gain. Critically, since the computational complexity of the CFAR detection algorithms is low and

comparable to that of the ABF the proposed algorithms can be ran in quasi-real time.

BIBLIOGRAPHY

[1] R. Klemm, "Adaptive clutter suppression for airborne phased array radars," *Microwaves, Optics and Antennas, IEE Proceedings H*, vol. 130, pp. 125–132, Feb. 1983.

[2] T. J. Nohara, P. Weber, A. Premji, and T. Bhattacharya, "Airborne ground moving target indication using non-side-looking antennas," in *IEEE Radar Conf.*, Dallas, TX, 1998, pp. 269–274.

[3] J. N. Entzminger, C. A. Fowler, and W. J. Kenneally, "Jointstars and GMTI: Past, present and future," *IEEE Trans. on Aerospace and Electron. Syst.*, vol. 35, no. 2, pp. 748–761, Apr. 1999.

[4] P. M. Corbell, J. J. Perez, and M. Rangaswamy, "Enhancing GMTI performance in non-stationary clutter using 3d STAP," in *Proc. IEEE Radar Conf.*, Boston, MA, 2007, pp. 647–652.

[5] D. J. Rabideau and S. M. Kogon, "A signal processing architecture for space-based GMTI radar," in *Proc. Radar Conf.*, Waltham, MA, Apr. 1999, pp. 96–101.

[6] J. Ward, "Space-time adaptive processing for airborne radar," MIT Lincoln Laboratory, Lexington, MA, Tech. Rep. 1015, Dec. 1994.

[7] J. R. Guerci, *Space-time adaptive processing for radar.* Norwood, MA: Artech House, 2003.

[8] L. E. Brennan and L. Reed, "Theory of adaptive radar," *IEEE Trans. on Aerospace and Electron. Syst.*, vol. AES-9, no. 2, pp. 237–252, Mar. 1973.

[9] J. Ward, "Space-time adaptive processing with sparse antenna arrays," in *Proc. 32nd Asilomar Conf. on Signals, Syst., and Comput.*, Pacific Grove, CA, Nov. 1998, pp. 1537–1541.

[10] T. K. Sarkar, H. Wang, S. Park, R. Adve, J. Koh, K. Kim, Y. Zhang, M. C. Wicks, and R. D. Brown, "A deterministic least-squares approach to space-time adaptive processing (STAP)," *IEEE Trans. on Antennas and Propagation*, vol. 49, no. 1, pp. 91–103, Jan. 2001.

[11] R. Klemm, *Principles of space-time adaptive processing.* London, U.K.: IEE Press, 2002.

[12] E. Brookner, *Radar technology.* Dedham, MA: Artech, 1977.

[13] H. L. Van Trees, *Detection, estimation, and modulation theory, Part IV Optimum Array Processing.* New York: Wiley Interscience, 2002.

[14] R. J. Mailloux, *Phased array antenna handbook*. New York: Artech House Inc., 1994.

[15] B. D. Van Veen and K. M. Buckley, "Beamforming: A versatile approach to spatial filtering," *IEEE ASSP Mag.*, vol. 5, no. 2, pp. 4–24, Apr. 1988.

[16] J. Capon, "High-resolution frequency-wavenumber spectrum analysis," *Proc. of the IEEE*, vol. 57, no. 8, pp. 1408–1418, Aug. 1969.

[17] R. Schmidt, "Multiple emitter location and signal parameter estimation," *IEEE Trans. on Antennas and Propagation*, vol. 34, no. 3, pp. 276–280, Mar. 1986.

[18] B. Friedlander, "The root-MUSIC algorithm for direction finding with interpolated arrays," *Europ. J. Signal Process.*, vol. 30, pp. 15–29, 1993.

[19] B. D. Rao and K. Hari, "Performance analysis of root-MUSIC," *IEEE Trans. on Acoust., Speech, and Signal Process.*, vol. 37, no. 12, pp. 1939–1949, Dec. 1989.

[20] R. Roy and T. Kailath, "ESPRIT-estimation of signal parameters via rotational invariance techniques," *IEEE Trans. on Acoust., Speech, and Signal Process.*, vol. 37, no. 7, pp. 984–995, Jul. 1989.

[21] B. Ottersten, M. Viberg, and T. Kailath, "Performance analysis of the total least squares ESPRIT algorithm," *IEEE Trans. on Signal Process.*, vol. 39, no. 5, pp. 1122–1135, May 1991.

[22] F.-M. Han and X.-D. Zhang, "An ESPRIT-like algorithm for coherent DOA estimation," *IEEE Antennas and Wireless Propagation Letters*, vol. 4, pp. 443–446, 2005.

[23] J. Rissanen, "A universal prior for integers and estimation by minimum description length," *The Annals of Statistics*, vol. 11, no. 2, pp. 416–431, Jun. 1983.

[24] M. Wax and T. Kailath, "Detection of signals by information theoretic criteria," *IEEE Trans. on Acoust., Speech, and Signal Process.*, vol. 33, no. 2, pp. 387–392, Apr. 1985.

[25] L. Huang, S. Wu, and X. Li, "Reduced-rank MDL method for source enumeration in high-resolution array processing," *IEEE Trans. on Signal Process.*, vol. 55, no. 12, pp. 5658–5667, Dec. 2007.

[26] E. Fishler, A. Haimovich, R. Blum, D. Chizhik, L. Cimini, and R. Valenzuela, "MIMO radar: an idea whose time has come," in *Proc. IEEE Radar Conf.* Philadelphia, PA: IEEE, 2004, pp. 71–78.

[27] E. Fishler, A. Haimovich, R. Blum, R. Cimini, D. Chizhik, and R. Valenzuela, "Performance of MIMO radar systems: advantages of angular diversity," in *Proc. 32nd Asilomar Conf. on Signals, Syst., and Comput.* Pacific Grove, CA: IEEE, Nov. 2004, pp. 305–309.

[28] J. Li and P. Stoica, "MIMO radar with colocated antennas," *IEEE Signal Process. Mag.*, vol. 24, no. 5, pp. 106–114, Sep. 2007.

[29] D. Bliss, K. Forsythe, S. Davis, G. Fawcett, D. Rabideau, L. Horowitz, and S. Kraut, "GMTI MIMO radar," in *Proc. Waveform Diversity and Design Conf.*, Feb. 2009, pp. 118–122.

[30] C.-Y. Chen and P. P. Vaidyanathan, "MIMO radar space–time adaptive processing using prolate spheroidal wave functions," *IEEE Trans. on Signal Process.*, vol. 56, no. 2, pp. 623–635, Feb. 2008.

[31] J. Li and P. Stoica, *MIMO radar signal processing.* New York: Wiley Online Library, 2009.

[32] Y. Lo, "A mathematical theory of antenna arrays with randomly spaced elements," *IEEE Trans. on Antennas and Propagation*, vol. 12, no. 3, pp. 257–268, May 1964.

[33] V. Agrawal and Y. Lo, "Mutual coupling in phased arrays of randomly spaced antennas," *IEEE Trans. on Antennas and Propagation*, vol. 20, no. 3, pp. 288–295, May 1972.

[34] B. Steinberg, "The peak sidelobe of the phased array having randomly located elements," *IEEE Trans. on Antennas and Propagation*, vol. 20, no. 2, pp. 129–136, Mar. 1972.

[35] B. D. Steinberg, *Principles of aperture and array system design: Including random and adaptive arrays*, New York, 1976.

[36] M. Rossi, A. M. Haimovich, and Y. C. Eldar, "Spatial compressive sensing in MIMO radar with random arrays," in *Proc. 46th Conf. on Inform. Sci. and Syst.*, Princeton, NJ, 2012, pp. 1–6.

[37] ——, "Spatial compressive sensing for MIMO radar," *IEEE Trans. on Signal Process.*, vol. 62, no. 2, pp. 419–430, Jan. 2014.

[38] F. Athley, C. Engdahl, and P. Sunnergren, "On radar detection and direction finding using sparse arrays," *IEEE Trans. on Aerospace and Electron. Syst.*, vol. 43, no. 4, pp. 1319–1333, Oct. 2007.

[39] D. L. Donoho, "Compressed sensing," *IEEE Trans. on Inform. Theory*, vol. 52, no. 4, pp. 1289–1306, Apr. 2006.

[40] R. G. Baraniuk, "Compressive sensing," *IEEE Signal Process. Mag.*, vol. 24, no. 4, Jul. 2007.

[41] D. Malioutov, M. Çetin, and A. S. Willsky, "A sparse signal reconstruction perspective for source localization with sensor arrays," *IEEE Trans. on Signal Process.*, vol. 53, no. 8, pp. 3010–3022, Aug. 2005.

[42] M. Herman and T. Strohmer, "Compressed sensing radar," in *Proc. IEEE Radar Conf.* Rome: IEEE, 2008, pp. 1–6.

[43] M. A. Herman and T. Strohmer, "High-resolution radar via compressed sensing," *IEEE Trans. on Signal Process.*, vol. 57, no. 6, pp. 2275–2284, Jun. 2009.

[44] R. Tibshirani, "Regression shrinkage and selection via the lasso," *J. of the Roy. Statistical Soc. B*, vol. 58, no. 1, pp. 267–288, 1996.

[45] S. S. Chen, D. L. Donoho, and M. A. Saunders, "Atomic decomposition by basis pursuit," *SIAM Review*, vol. 43, no. 1, pp. 129–159, 2001.

[46] J. M. Bioucas-Dias and M. A. Figueiredo, "A new twist: two-step iterative shrinkage/thresholding algorithms for image restoration," *IEEE Trans. on Image Process.*, vol. 16, no. 12, pp. 2992–3004, Dec. 2007.

[47] D. L. Donoho, A. Maleki, and A. Montanari, "Message-passing algorithms for compressed sensing," *Proc. of the Nat. Academy of Sciences*, vol. 106, no. 45, pp. 18 914–18 919, 2009.

[48] A. Beck and M. Teboulle, "A fast iterative shrinkage-thresholding algorithm for linear inverse problems," *SIAM J. on Imaging Sciences*, vol. 2, no. 1, pp. 183–202, 2009.

[49] I. W. Selesnick, S. U. Pillai, K. Y. Li, and B. Himed, "Angle-doppler processing using sparse regularization," in *Proc. IEEE Int. Conf. on Acoustics, Speech, and Signal Process. (ICASSP)*, Dallas, TX, 2010, pp. 2750–2753.

[50] L. Anitori, A. Maleki, M. Otten, R. G. Baraniuk, and P. Hoogeboom, "Design and analysis of compressed sensing radar detectors," *IEEE Trans. on Signal Process.*, vol. 61, no. 4, pp. 813–827, Feb. 2013.

[51] N. A. Goodman and L. C. Potter, "Pitfalls and possibilities of radar compressive sensing," *Applied optics*, vol. 54, no. 8, pp. C1–C13, 2015.

[52] J. A. Tropp and A. C. Gilbert, "Signal recovery from random measurements via orthogonal matching pursuit," *IEEE Trans. on Inform. Theory*, vol. 53, no. 12, pp. 4655–4666, Dec. 2007.

[53] W. Dai and O. Milenkovic, "Subspace pursuit for compressive sensing: Closing the gap between performance and complexity," *IEEE Trans. on Inform. Theory*, vol. 55, no. 5, pp. 2230–2249, May 2009.

[54] D. Needell and J. A. Tropp, "Cosamp: Iterative signal recovery from incomplete and inaccurate samples," *Appl. and Computational Harmonic Anal.*, vol. 26, no. 3, pp. 301–321, 2009.

[55] M. Rossi, A. M. Haimovich, and Y. C. Eldar, "Compressive sensing with unknown parameters," in *Proc. 46th Asilomar Conf. on Signals, Syst., and Comput.* IEEE, 2012, pp. 436–440.

[56] M. E. Davies and Y. C. Eldar, "Rank awareness in joint sparse recovery," *IEEE Trans. on Inform. Theory*, vol. 58, no. 2, pp. 1135–1146, Feb 2012.

[57] M. Elad, *Sparse and Redundant Representations: From Theory to Applications in Signal and Image Processing.* New York: Springer, 2010.

[58] H. H. Kim, M. A. Govoni, and A. M. Haimovich, "Cost analysis of compressive sensing for MIMO STAP random arrays," in *Proc. IEEE Radar Conf.*, Arlington, VA, 2015, pp. 0980–0985.

[59] Y. Chi, L. L. Scharf, A. Pezeshki, and A. R. Calderbank, "Sensitivity to basis mismatch in compressed sensing," *IEEE Trans. on Signal Process.*, vol. 59, no. 5, pp. 2182–2195, May 2011.

[60] M. Herrman and T. Strohmer, "General perturbations of sparse signals in compressed sensing," in *Proc. Int. Conf. Sampling Thoery and Appl. (SAMPTA)*, Marseille, France, 2009, pp. General–session.

[61] M. A. Herman and T. Strohmer, "General deviants: An analysis of perturbations in compressed sensing," *IEEE J. Sel. Topics in Signal Process.: Special Issue on Compressive Sens.*, vol. 4, no. 2, pp. 342–349, Apr. 2010.

[62] G. Tang, B. N. Bhaskar, P. Shah, and B. Recht, "Compressed sensing off the grid," *IEEE Trans.s on Inform. Theory*, vol. 59, no. 11, pp. 7465–7490, Nov. 2013.

[63] Y. Chen and Y. Chi, "Robust spectral compressed sensing via structured matrix completion," *IEEE Trans. Inf. Theory*, no. 10, pp. 6576–6601, Oct. 2014.

[64] Z. Yang, L. Xie, and C. Zhang, "Off-grid direction of arrival estimation using sparse bayesian inference," *IEEE Trans. on Signal Process.*, vol. 61, no. 1, pp. 38–43, Jan. 2013.

[65] Y. Chi and Y. Chen, "Compressive recovery of 2-d off-grid frequencies," in *Proc. Asilomar Conf. on Signals, Syst. and Comput.*, Pacific Grove, CA, 2013, pp. 687–691.

[66] Y. Chi, "Joint sparsity recovery for spectral compressed sensing," in *Proc. IEEE Int. Conf. on Acoust., Speech and Signal Process. (ICASSP)*, 2014, pp. 3938–3942.

[67] H. Jamali-Rad and G. Leus, "Sparsity-aware multi-source TDOA localization," *IEEE Trans. on Signal Process.*, vol. 61, no. 19, pp. 4874–4887, Oct. 2013.

[68] Y. Li and Y. Chi, "Off-the-grid line spectrum denoising and estimation with multiple measurement vectors," *IEEE Trans. on Signal Process.*, vol. 64, no. 5, pp. 1257–1269, Mar. 2016.

[69] V. Chandrasekaran, B. Recht, P. A. Parrilo, and A. S. Willsky, "The convex geometry of linear inverse problems," *Found. of Computational Math.*, vol. 12, no. 6, pp. 805–849, 2012.

[70] B. Eisenberg, "On the expectation of the maximum of IID geometric random variables," *Statistics and Probability Letters*, vol. 78, no. 2, pp. 135–143, 2008.

[71] L. Brennan and F. Staudaher, "Subclutter visibility demonstration," Technical Report RL-TR-92-21, Adaptive Sensors Inc., Tech. Rep., 1992.

[72] E. J. Kelly, "An adaptive detection algorithm," *IEEE Trans. on Aerospace and Electron. Syst.*, no. 2, pp. 115–127, Mar. 1986.

[73] F. C. Robey, D. R. Fuhrmann, E. J. Kelly, and R. Nitzberg, "A CFAR adaptive matched filter detector," *IEEE Trans. on Aerospace and Electron. Syst.*, vol. 28, no. 1, pp. 208–216, Jan. 1992.

[74] I. S. Reed, J. D. Mallett, and L. E. Brennan, "Rapid convergence rate in adaptive arrays," *IEEE Trans. on Aerospace and Electronic Syst.*, no. 6, pp. 853–863, Nov. 1974.

[75] E. Kelly, "Performance of an adaptive detection algorithm; rejection of unwanted signals," *IEEE Trans. on Aerospace and Electron. Syst.*, vol. 25, no. 2, pp. 122–133, Mar. 1989.

[76] D. M. Boroson, "Sample size considerations for adaptive arrays," *IEEE Trans. on Aerospace and Electron. Syst.*, vol. AES-16, no. 4, pp. 446–451, Jul. 1980.

[77] R. T. Behrens and L. L. Scharf, "Signal processing applications of oblique projection operators," *IEEE Trans. on Signal Process.*, vol. 42, no. 6, pp. 1413–1424, Jun. 1994.

[78] L. L. Scharf and B. Friedlander, "Matched subspace detectors," *IEEE Trans. on Signal Process.*, vol. 42, no. 8, pp. 2146–2157, Aug. 1994.

[79] G. H. Golub and C. F. Van Loan, *Matrix computations*. Baltimore, MD: The John Hopkins Press, 2012.